Tokyo University of Science

Doctoral thesis

Studies on Mott-Related Phenomena in Quasi-Two-Dimensional Organic Conductors

（擬二次元有機導体を用いたモット転移周りの物理現象の研究）

Riku Yamamoto

（山本　陸）

Department of Applied Physics, Tokyo University of Science

6-3-1 Niijuku, Katsushika, Tokyo 125-8585, Japan

March 2021

Contents

1 General Introduction 1

1.1 Strongly correlated electron systems 1

1.1.1 Mott insulator and Mott transition 2
1.1.2 How to induce Mott transitions 5
1.1.3 The universality class of the Mott transition 6

1.2 Organic conductors 7

1.2.1 Low dimensionality 7
1.2.2 Strongly correlated system 7
1.2.3 Advantages 8
1.2.4 κ-$(ET)_2X$ 9
1.2.5 $Y[Pd(dmit)_2]_2$ 10

1.3 Organization of thesis 12

2 Dimensionality of Superconductivity in $EtMe_3P[Pd(dmit)_2]_2$ under pressure 13

2.1 Introduction 14

2.1.1 $EtMe_3P[Pd(dmit)_2]_2$ and Purpose 15
2.1.2 Layered superconductors 17

2.2 Experiment 18

2.2.1 Samples 18
2.2.2 Applying pressure 18
2.2.3 AC susceptibility measurement 19

2.3 Results and Discussion 21
2.3.1 Diamagnetic signal under H_{dc} = 0 T 21
2.3.2 Angle dependence of the diamagnetic signal 23
2.3.3 Temperature dependence of the upper critical fields 25
2.3.4 Angle dependence of the transition temperature 28
2.3.5 The molecular orbital 31
2.4 Conclusion 32
3 Electronic Griffiths Phase in x-ray irradiated κ-$(ET)_2Cu[N(CN)_2]Cl$ 33
3.1 Introduction 34
3.1.1 Hierarchy of energy and length scales in physics 34
3.1.2 Purpose and κ-$(ET)_2Cu[N(CN)_2]Cl$ 36
3.2 Experiment 39
3.2.1 Samples 39
3.2.2 X-ray irradiation 39
3.2.3 Applying pressure 39
3.2.4 NMR 40
3.3 Results and Discussion 48
3.3.1 Spectra 48
3.3.2 Spin-lattice relaxation rate T_1^{-1} 50
3.3.3 Spin-spin relaxation rate T_2^{-1} 53
3.3.4 Contribution of ethylene-group dynamics 55
3.3.5 Contribution of domain wall dynamics 57
3.3.6 Proposal for the concept of the electronic Griffiths phase 58
3.3.7 Expansion of the concept of the electronic Griffiths phase 60
3.4 Conclusion 62
4 Concluding Remarks 63

1 General Introduction

The discovery of the high-T_c (superconducting critical transition temperature) superconductivity in cuprates [1] triggered the rapid development of the field of "strongly correlated electron systems", and the field has become one of the most important fields of solid-state (condensed matter) physics. A variety of studies has established understandings of properties for many groups of materials, such as cuprates, manganites, and organic conductors. However, understanding of the metal-insulator transition − *Mott transition* − and the physics around it, which are fundamental issues in strongly correlated electron systems, remains incomplete. I have focused on organic conductors to give insights into these issues. In this chapter, I will describe the features of the strongly correlated electron systems and the organic conductors and clarify why I have focused on the organic conductors.

1.1 Strongly correlated electron systems

Strongly correlated electron systems are realized when the band theory breaks down owing to Coulomb repulsion between electrons. When the Coulomb repulsion is weak and the one-particle approximation can be valid, the band theory is well justified. This theory successfully classifies the electronic states of materials into two groups, namely, metallic and insulating states; when a system has an incompletely filled band, the system shows a metallic state; when a system only has bands that are completely filled or empty, the system shows an insulating state. The metallic state with *weak* Coulomb repulsion between electrons, which can be treated as a perturbation, is described by the "Landau Fermi liquid theory" except for one-dimensional systems and is called the *Fermi liquid state*.

In the strongly correlated electron systems, *strong* Coulomb repulsion breaks the above mentioned one-particle approximation and leads the physics to the many-body problem of electrons. The systems with *strong* Coulomb repulsion show insulating states that are essentially different from the insulating state described by the band theory; the electrons are localized because of the strong Coulomb repulsion.

1.1.1 Mott insulator and Mott transition

I will consider the case where the charge density defined as the ratio of electron number to site number is unity (N = 1), as in the solid hydrogen. I discuss the electronic state of this system as a function of the absolute value of the ratio of the transfer integral t (t < 0) to the on-site Coulomb repulsion U (> 0), $|U/t|$. When $|U/t|$ is small, the system shows a half-filled band metallic state (Fermi liquid state). When $|U/t|$ is large enough, it shows an insulating state different from the insulating state described by the band theory, which is called a "*Mott insulator.*" A transition between these states (the half-filled band metallic state and Mott insulator) owing to the Coulomb repulsion as described above is called a "*Mott transition.*"

The minimal model Hamiltonian (single-band Hubbard Hamiltonian) describing the Mott insulator ($|U/t| >> 1$) is written as

$$\mathcal{H} = t\sum_{\langle i,j\rangle\sigma}\left(c_{i\sigma}^{\dagger}c_{j\sigma} + \text{h. c.}\right) + U\sum_{i} n_{i\uparrow}n_{i\downarrow}, \tag{1-1}$$

where σ is a spin index which takes ↑ (S_z = 1/2) and ↓ (S_z = –1/2), i represents the site, $n_{i\sigma}$ (= $c^{\dagger}_{i\sigma}$ $c_{i\sigma}$) and $c^{\dagger}_{i\sigma}$ ($c_{i\sigma}$) denote number operator and creation (annihilation) operators for the particle with σ spin at i th site, respectively. When U is much larger than t, the single-particle spectrum split into the lower and upper Hubbard bands, and the Hubbard gap (~U) appears between the Hubbard bands; the particles cannot itinerate between sites, and they are localized at each site due to the strong Coulomb repulsion. In the Mott insulators, the spin degree of freedom survives because one particle is localized at each site. Dealing with the first term in Eq. (1-1) as a second-order perturbation, we obtain the effective Hamiltonian describing the spin degrees of freedom:

$$\mathcal{H}_{\text{eff}} = 2J\sum_{i}(\boldsymbol{S}_i \cdot \boldsymbol{S}_{i+1} - \tfrac{1}{4}),$$

$$J \equiv \tfrac{2t^2}{U} \ (> 0). \tag{1-2}$$

This effective Hamiltonian is well known as the antiferromagnetic Heisenberg Hamiltonian. Thus, the Mott insulators usually have an antiferromagnetic interaction between the spins.

Two scenarios have been discussed for a long time to describe the Mott transition. One is the Hubbard scenario [2]. In the Hubbard scenario, with increasing $|U/t|$ from the Fermi liquid side, the single-particle spectrum gradually splits into the lower and upper Hubbard bands (Fig. 1.1(a)). The other is the Brinkman-Rice scenario [3]. In the Brinkman-Rice scenario, with increasing $|U/t|$ from the Fermi liquid side, the bandwidth of the single-particle spectrum becomes narrow, and the lower and

upper Hubbard bands appear eventually (Fig. 1.1(b)). This spectral narrowing and appearing of these Hubbard bands suggest that an effective mass of the particle (inverse of quasiparticle weight) becomes heavier, and thus diverges at the critical point. These two scenarios conflicted with each other.

After that, Zhang *et al*. proposed a dynamic mean-field theory (DMFT) for the Mott transition and successfully treated these two scenarios in a unified manner [4]. Note that, this DMFT is justified in infinite-dimensional systems and may not be fully valid in lower dimensional systems. In the DMFT scenario, with increasing $|U/t|$ from the Fermi liquid side, both splitting of the single-particle spectrum and narrowing of the spectrum-width are realized as shown in Fig. 1.1(c). This suggests that both the Hubbard and Brinkman-Rice scenarios shed light only on one aspect of the Mott transition. Therefore, the appearance of the two Hubbard bands and the divergence of the effective masses of particles are likely to be important factors in the Mott transition.

For $0 < N < 2$ except $N = 1$, systems also sometimes show metal-insulator transition, and the transition and the resulting insulator are also called a Mott transition and a Mott insulator, respectively. Note that this Mott transition cannot be described by the simple Mott-Hubbard Hamiltonian. The precise description of the transition is still under debate.

The Mott transition systems show a variety of novel phenomena, such as the high-T_c superconductivity, giant magnetoresistive effect, and quantum spin liquid. The variety of electronic states is believed to be caused by competing effects between the many-body effect and various factors, such as phonon, frustration, and randomness.

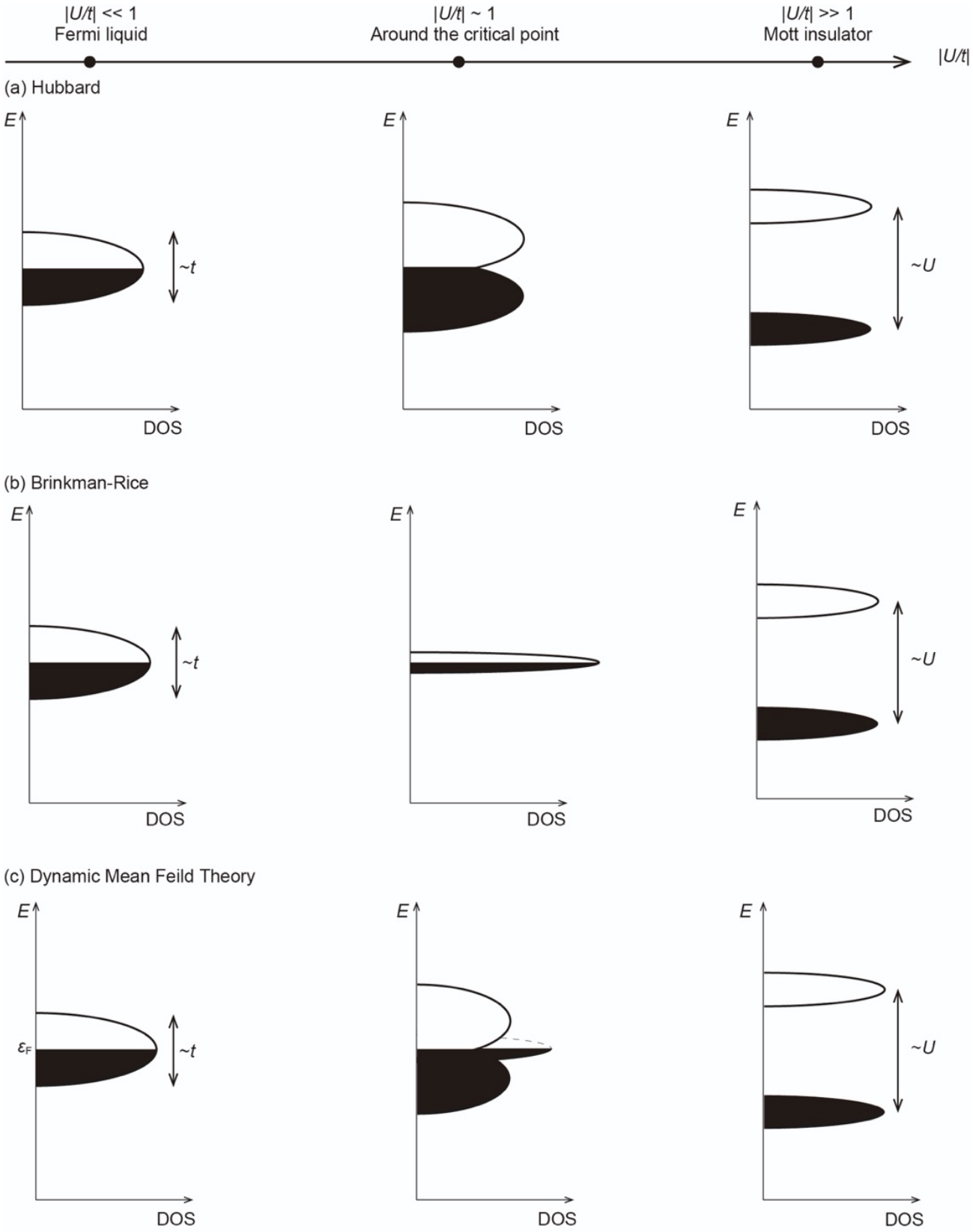

Fig. 1.1. Schematic three scenarios of Mott transition

1.1.2 How to induce Mott transitions

There are two types of Mott transition (Fig. 1.2). One is called a “bandwidth-controlled Mott transition.” This Mott transition can be induced by changing a lattice parameter and controlling the overlap of wave functions (transfer integral). There are two known methods to change the lattice parameter: one is to apply external pressure, and the other is to change the chemical composition and thus apply chemical pressure. The other is called a “filling-controlled Mott transition.” The Mott transition is caused by career doping (introducing electrons or holes and changing the band filling)

.

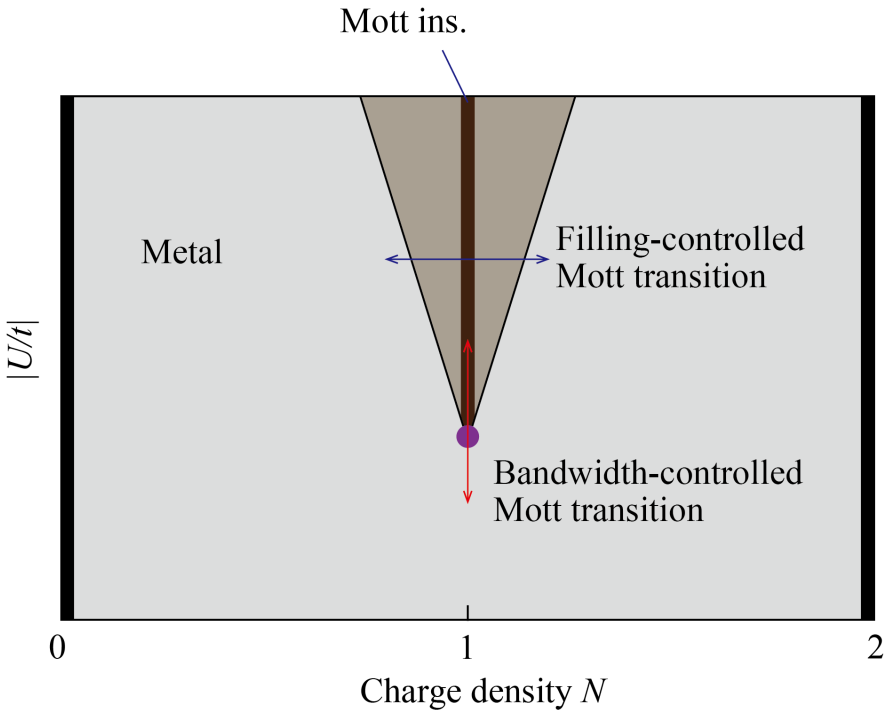

Fig. 1.2. The bandwidth-controlled and filling-controlled Mott transitions

1.1.3 The universality class of the Mott transition

The Mott transition (bandwidth-controlled Mott transition) is known as a first-order transition with a finite-temperature critical endpoint in the pressure (namely, $|t/U|$) – temperature phase diagram. Theoretical works suggest that the Mott transition described by the half-filled Hubbard Hamiltonian belongs to the Ising universality class; Castellani *et al.* obtained an effective Hamiltonian from the half-filled Hubbard Hamiltonian and found that the transition can be treated by analogy to the gas-liquid transition, which belongs to the Ising universality class [5]; Kotliar *et al.* used a DMFT for Hubbard Hamiltonian and also found that the Mott transition belongs to the Ising universality class [6,7]. From the experimental point of view, Limelette *et al.* obtained the critical behavior of the conductivity near the endpoint of the Mott transition of Cr-doped V_2O_3 and found that the Mott transition belongs to the Ising universality class, consistent with the theoretical works [8]. Besides, Imada studied a phenomenological theory and suggested that when the temperature of the endpoint of a Mott transition is much higher than the energy scale of the quantum degeneracy, it belongs to the Ising universality class, but when they are close, it belongs to an unconventional universality class [9]. Indeed, from the experimental point of view, Kagawa *et al.* obtained the critical behavior of the conductivity near the endpoint of the Mott transition of the organic conductor κ-$(ET)_2X$ system and claimed that the Mott transition in the material belongs to the unconventional universality class [10]. However, this experimental result is still under debate. Papanikolaou *et al.* presented a unified phenomenological description of all the experimental facts within an Ising-type model and pointed out that the critical behavior of the conductivity of κ-$(ET)_2X$ can be explained by the Ising universality class [11]. Besides, Bartosch *et al.* developed a scaling theory for describing the singular part of the thermodynamic expansivity in the vicinity of a finite-temperature critical endpoint [12]. Together with the results of the thermal measurements of κ-$(ET)_2X$ [13], they claimed that the Mott transition of κ-$(ET)_2X$ belongs to the conventional Ising universality class in their theory [12]. Recently, Abdel-Jawad *et al.* obtained the critical behavior of the conductivity and thermoelectric power near the endpoint of the Mott transition of the organic conductor $EtMe_3P[Pd(dmit)_2]_2$ and claimed that the Mott transition of $EtMe_3P[Pd(dmit)_2]_2$ belongs to the Ising universality class [14]. Therefore, the universality class of the Mott transition is still under debate, but at least it is believed that the universality class relates to the Ising universality class.

1.2 Organic conductors

In solid-state physics, organic conductors, which are constructed of organic molecules, have been regarded as ideal playgrounds to study the low-dimensional correlated-electron physics. Low-dimensional physics is attractive because synergistic effects between the low dimensionality and various interactions produce interesting physical phenomena, such as the high-T_c superconductivity, the charge density wave, and the quantized Hall effect. This is because in high-dimensional systems, these effects are averaged out and peculiar properties due to these effects do not appear. However, in low-dimensional systems, peculiar properties can appear because the averaging effect is suppressed due to the low dimensionality. Besides, $|U/t|$ is relatively large in the organic conductors as explained in the subsect. 1.1.1, and thus they are also ideal playgrounds for the strongly correlated electron systems.

1.2.1 Low dimensionality

The low dimensionality in the organic conductors is due to the anisotropic shape of molecules that constitutes the organic conductors. In many cases, the molecules do not have spherical symmetry, and thus cause a strong anisotropy of the materials. Besides, frontier electron orbitals (HOMO: Highest Occupied Molecular Orbital, and LUMO: Lowest Unoccupied Molecular Orbital) in the materials, which are responsible for electrical conduction, are constituted by π-orbitals. The π-orbitals also have an anisotropy. Thus, these features restrict the dynamics of the electrons to a lower dimension.

1.2.2 Strongly correlated system

The relatively large value of $|U/t|$ in the organic conductors is due to the composition of the matter. The organic conductors are formed by a van der Waals force between molecules, which is much weaker than the force that forms covalent bonds between atoms. Thus, lattice constants in the organic conductors become larger than those in inorganic materials, and transfer integrals between molecules are smaller than those between atoms in inorganic materials. In the organic conductors, therefore, the bandwidth becomes narrow compared to inorganic materials and is comparable with an on-site Coulomb repulsion.

1.2.3 Advantages

There are several advantages of organic conductors to study low-dimensional strongly correlated electron systems. The main advantages are (i) cleanliness and (ii) high controllability of various parameters. (i) Organic conductors are clean systems. In inorganic materials, one atom plays the role of one lattice point. Inorganic materials easily have vacancies in the atomic sites, and thus undesirable lattice defects are easily created. In organic conductors, one molecule plays the role of one lattice point. The molecules are rarely gone because they are tens of times larger than atoms. It is believed that such large components are unlikely to go away. Thus, organic conductors hardly have undesirable lattice vacancies and allow studying physics without undesirable uncontrolled randomness. (ii) Organic conductors have high controllability of various parameters. The parameters that can be easily controlled are as follows: transfer integrals by the external pressure and the chemical pressure, randomness by cooling rate and x-ray irradiation; carrier doping by a field-effect transistor configuration.

The controllability of transfer integrals by the external pressure is owing to the softness of organic conductors. As described in the subsect. 1.2.2, organic conductors are formed by the weak van der Waals force. Owing to the weak force, organic conductors are several times softer than inorganic systems; and thus, external pressure can easily control the distance between the molecules, or the transfer integrals between the molecules. Besides, changing the chemical composition can apply chemical pressure.

The controllability of randomness is owing to the properties of molecules. Molecules sometimes take several molecular-shape conformations at high temperatures and fluctuate between them. When organic conductors are cooled rapidly, the molecules take meta-stable conformations, causing quenched disorder. Besides, x-ray irradiation also can introduce quenched disorder because it causes molecule defects that can hardly be repaired. These methods of introduction of randomness allow systematic studying of strongly correlated electron systems with intentional randomness.

Recently, the method of doping to organic conductors has been developed [15]. The method uses a field-effect transistor configuration. This method has been well-established in inorganic materials, but now it can be applied to organic conductors as well, making more comprehensive research possible; the method for organic conductors makes it possible to study the doping effect for a pure system without undesirable randomness in contrast to inorganic materials.

Thus, organic conductors provide ideal playgrounds for a comprehensive understanding of the physics of strongly correlated electron systems because of these advantages.

1.2.4 κ-$(ET)_2X$

Among several quasi-two-dimensional organic conductors, κ-$(ET)_2X$ systems (where ET (Fig. 1.3(a)) is the abbreviation of BEDT-TTF: (bis(ethylenedithio)tetrathiafulvalene) and X is an anion, such as X= $Cu[N(CN)_2]Cl$, $Cu[N(CN)_2]Br$, $Cu(NCS)_2$, and $Cu_2(CN)_3$) have been especially intensively studied [16]. The κ-$(ET)_2X$ systems have a layered structure; a conducting ET layer is segregated by a nonmagnetic insulating anion layer X. The κ-$(ET)_2X$ systems are charge transfer salts; one ET dimer provides one electron to the anion X. Thus, the HOMO band of the κ-$(ET)_2X$ systems becomes half-filled. The ET dimer plays the role of one lattice point of a triangular lattice, and an effective single-band Hubbard Hamiltonian with on-site Coulomb repulsion U and transfer integrals t between the ET dimers can describe the fundamental properties of the system [17]. When $|U/t|$ is large, this system shows a dimer Mott insulating state. In the Mott insulating state, the spin state usually undergoes antiferromagnetic long-range ordering at low temperatures [18]. The exception is X = $Cu_2(CN)_3$, where the effect of strong geometric frustration results in a quantum spin liquid state [19,20]. When U/t is small, this system shows a half-filled metallic state (Fermi liquid state). In addition, at low temperatures, the system shows superconductivity near the Mott boundary [21,22], which is believed to have d-wave nature [23-27]. The $|U/t|$ can be controlled by applying pressure or chemical pressure, as described in the subsect. 1.1.2. The phase diagram of the κ-$(ET)_2X$ system is shown in Fig.1.4(a), and κ-$(ET)_2X$ systems show a Mott transition with a critical endpoint, as described in the subsect. 1.1.3

The superconductivity in the κ-$(ET)_2X$ systems is usually adjacent to the antiferromagnetic long-range ordered state, which is similar to the high-T_c cuprates. The similarity of superconductivities in the κ-$(ET)_2X$ systems and the high-T_c cuprates, whose parent materials are Mott insulators, was pointed out [28]. Indeed, the energy scale for the κ-$(ET)_2X$ systems is about one-tenth smaller than that of the cuprates, and T_c of the κ-$(ET)_2X$ systems is also about one-tenth smaller than that of the cuprates. Note that there is a difference in the Mott transition. The Mott transition of the κ-$(ET)_2X$ systems is the bandwidth-controlled Mott transition, which is realized by external or chemical pressure [29,30]. The Mott transition of the cuprates is the filling-controlled Mott transition, which is realized by carrier doping.

The superconductivities in the κ-$(ET)_2X$ systems and the high-T_c cuprates are believed to be related to the antiferromagnetic Mott insulators and Mott transitions. A comprehensive understanding of Mott-related physics is required. However, inorganic materials, including the cuprates, inevitably have undesirable randomness and/or other effects, such as a Jahn-Teller effect and a spin-orbit coupling, and thus it is difficult to study pure Mott-related physics. In contrast, κ-$(ET)_2X$ is an appropriate system to study pure Mott-related physics because of the advantages as described in the subsect. 1.2.3.

1.2.5 $Y[Pd(dmit)_2]_2$

The organic conductors $Y[Pd(dmit)_2]_2$ systems (where Y is a cation, such as Y = $EtMe_3P$, $EtMe_3Sb$, Et_2Me_2P, where Et = C_2H_5, Me = CH_3, and dmit is 1,3-dithiol-2-thione-4,5-dithiolate, C_3S_5; Fig. 1.3(b)), which are similar to the κ-$(ET)_2X$ systems, have been attracted recently [16]. The $Y[Pd(dmit)_2]_2$ systems also have a layered structure and are quasi-two-dimensional systems; a conducting $Pd(dmit)_2$ layer is segregated by a nonmagnetic insulating cation Y layer. The $Y[Pd(dmit)_2]_2$ systems are charge transfer salts; one $Pd(dmit)_2$ dimer accepts one electron from the cation Y. Thus, the LUMO band of the $Y[Pd(dmit)_2]_2$ systems become half-filled. The $Pd(dmit)_2$ dimer plays the role of one lattice point of a triangular lattice. On-site Coulomb repulsions lead almost all $Y[Pd(dmit)_2]_2$ systems to Mott insulating states, as is similar to κ-$(ET)_2X$ systems. As for the spin degree of freedom, most of the $Y[Pd(dmit)_2]_2$ systems show an antiferromagnetic long-range ordered state at low temperatures, while it is believed that the ground states of $EtMe_3Sb[Pd(dmit)_2]_2$ and $EtMe_3P[Pd(dmit)_2]_2$ become a quantum spin liquid state and a valence bond solid (VBS) state, respectively, owing to the strong frustration effect in these two materials, which have nearly-equilateral triangular lattice transfer networks. The phase diagram of $EtMe_3P[Pd(dmit)_2]_2$ is shown in Fig. 1.4(b) as a representative example of the $Y[Pd(dmit)_2]_2$ systems [31,32]. Note that almost all $Y[Pd(dmit)_2]_2$ systems except $EtMe_3P[Pd(dmit)_2]_2$ show an antiferromagnetic ordered state instead of the VBS state. The $EtMe_3P[Pd(dmit)_2]_2$ system also shows a first-order Mott transition with a critical endpoint as described in the subsect. 1.1.3.

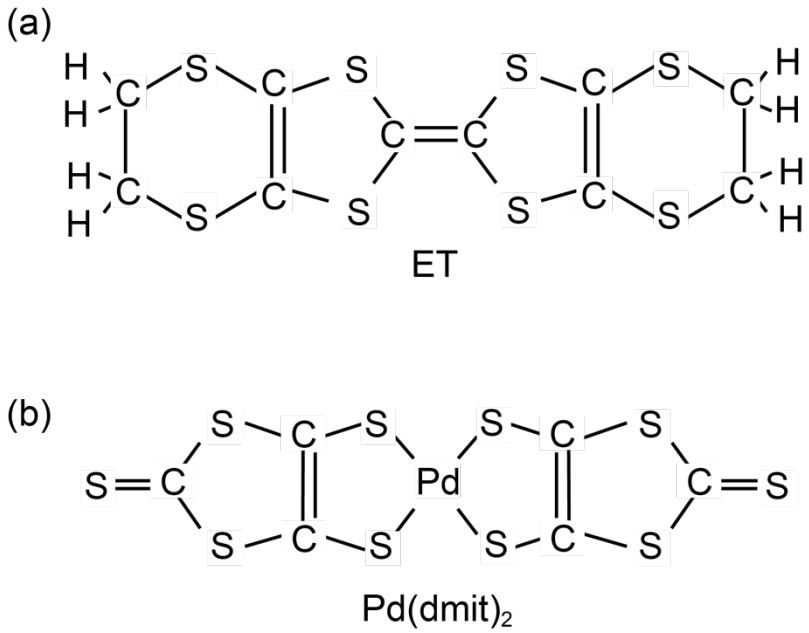

Fig.1.3. (a) ET and (b) $Pd(dmit)_2$ molecules.

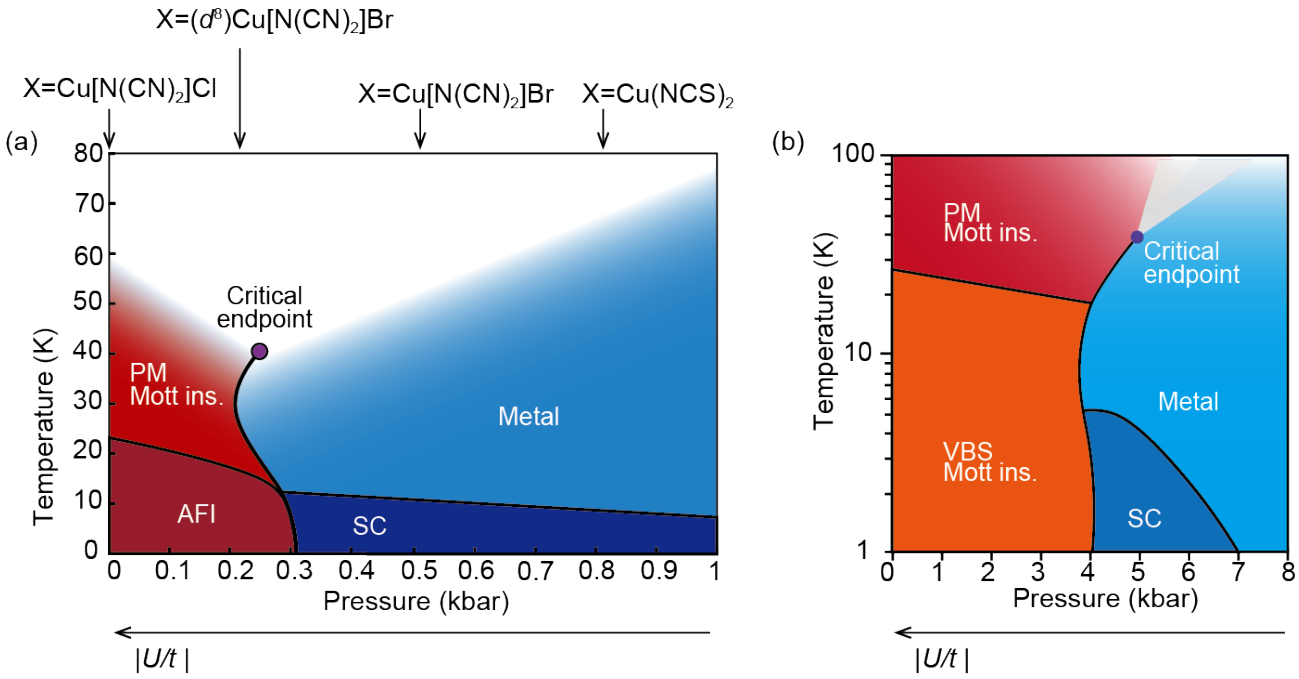

Fig. 1.4. The phase diagram of (a) κ-$(ET)_2X$ systems [21,22,29,30] and (b) $EtMe_3P[Pd(dmit)_2]_2$ [31,32]. (d^8) indicates that the ET molecule is fully deuterated. PM, AFI, VBS, and SC denote paramagnet, antiferromagnetic ordered insulator, valence bond solid, and superconductor, respectively. The pressure for (b) is defined at room temperature. At low temperatures, the pressure decreases by 1.5–2 kbar from that at room temperature.

1.3 Organization of thesis

There are two important open issues related to the Mott transition. One is superconductivity realized in the vicinity of the Mott transition. It has been widely known that unconventional superconductivity is realized around the Mott transition in many quasi-two-dimensional systems such as cuprates and organic materials. However, it is still unresolved what kind of superconductivity is realized when the dimensionality or lattice topology is varied. The other is the Mott transition itself. There is a consensus that, in clean systems, the Mott transition is a first-order transition at low temperatures with a critical endpoint in the pressure-temperature phase diagram, as I explained above. However, it is still unresolved what becomes of the Mott transition when randomness is introduced. Although these issues are fundamental and thus have been studied intensively in inorganic materials, they are still open issues even now.

In this thesis, I studied the two Mott-related physics, which are difficult to approach in inorganic materials, by focusing attention on organic conductors: a property of layered superconductivity located near the Mott transition, and a novel description of the Mott transition under randomness.

In chapter 2, I describe the study of the dimensionality of superconductivity in $EtMe_3P[Pd(dmit)_2]_2$, which has a quasi-two-dimensional triangular lattice. To study the property of the superconductivity, I performed ac magnetic susceptibility measurements for $EtMe_3P[Pd(dmit)_2]_2$ under pressure with a dc magnetic field applied perpendicular to the ac field. I investigated the dc field dependence of the ac susceptibility in detail and concluded that the superconductivity in $EtMe_3P[Pd(dmit)_2]_2$ is anisotropic three-dimensional superconductivity even at low temperatures, which contrasts with the large majority of other correlated electron layered superconductors such as high-T_c cuprates and κ-$(ET)_2X$ systems.

In chapter 3, I describe the study of a novel description of the Mott transition under randomness. To reveal the origin of the nature of the Mott transition under randomness, which has been discussed for a long time in the strongly correlated systems, I performed ^{13}C-NMR (nuclear magnetic resonance) measurements for the organic Mott transition system κ-$(ET)_2Cu[N(CN)_2]Cl$ under different three conditions. I found that a novel electronic state with extraordinary slow dynamics emerges only when the following two factors are met simultaneously: (i) the electronic system is near the metal/Mott-insulator boundary and (ii) the system is subject to quenched disorder. This electronic state under three conditions and the description of the Mott transition can be explained by the concept of the "(electronic) Griffiths phase."

In chapter 4, I summarized these studies conducted using organic materials and describe their significance and prospects.

2 Dimensionality of Superconductivity in $EtMe_3P[Pd(dmit)_2]_2$ under pressure

2.1 Introduction

Correlated-electron superconductivities on two-dimensional triangular lattices have attracted much theoretical attention. The correlated electron superconductors destabilize *s*-wave singlet superconductivity and thus often show *d*-wave singlet superconductivity. If the *d*-wave singlet superconductivity is on the triangular lattice, the three states related by the E_2 representation of the lattice symmetry (Fig. 2.1(a)) are degenerate and it is possible that a state described by a linear combination of these states ($d_{x^2-y^2} + id_{xy}$ wave chiral superconductivity) is realized (within the linear gap equation); Likewise, for *p*-wave triplet superconductivity (Fig. 2.1(b)), $p_x + ip_y$ wave superconductivity can be realized [33-37]. Note that the related three states are not linearly independent and a linear combination of two can create the other. From the experimental point of view, however, real materials for the correlated electron superconductivity on the triangular lattice are very limited. One of the few examples is the water-intercalated sodium cobalt oxide superconductor, $Na_xCoO_2{\cdot}yH_2O$, [38], which was studied very intensively. The experimental results on the superconductivity, however, still inconclusive [39–43] because the materials are strongly unstable concerning their chemical, structural, and thus superconducting properties [44,45].

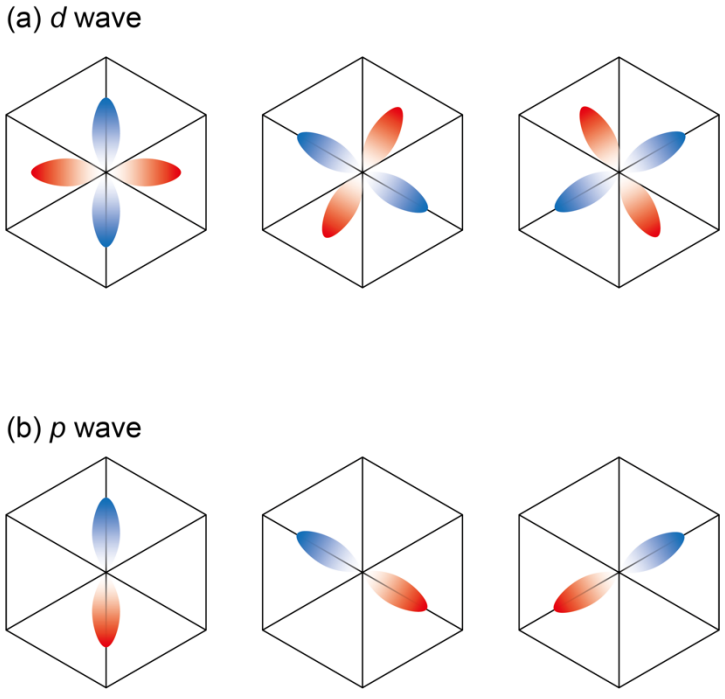

Fig. 2.1. The degenerated states related by the E_2 representation of the triangular lattice symmetry for (a) *d*-wave and (b) *p*-wave superconductivity.

2.1.1 $EtMe_3P[Pd(dmit)_2]_2$ and Purpose

Under such circumstances, a layered organic conductor, $EtMe_3P[Pd(dmit)_2]_2$ (space group $P2_{1/m}$; Figs. 2.2(a, b)) occupies an important position. In $EtMe_3P[Pd(dmit)_2]_2$, the $Pd(dmit)_2$ layer, which forms a quasi-two-dimensional electronic system, is segregated by a nonmagnetic insulating cation layer $EtMe_3P^+$. The family of $X[Pd(dmit)_2]_2$ has a triangular lattice of $[Pd(dmit)_2]_2$ dimers as shown in Fig. 2.2 (b). The three transfer integrals (t_b, t_s, and t_r in Fig. 2.2 (b)) on the three edges of the triangle are in principle different from one another in $X[Pd(dmit)_2]_2$ but they are almost equal in the $EtMe_3P[Pd(dmit)_2]_2$ system. Therefore, $EtMe_3P[Pd(dmit)_2]_2$ is considered as an electronic system with a nearly equilateral triangular lattice [46,47]. This system is a Mott insulator at ambient pressure because of the on-site Coulomb repulsion. When $EtMe_3P[Pd(dmit)_2]_2$ is pressurized, it undergoes a Mott transition and become a Fermi liquid state [31]. The Mott transition in the pressure-temperature phase diagram is a first-order transition with a critical endpoint (Fig. 1.4(b)) [31], as described in the subsect. 1.1.3. Besides, $EtMe_3P[Pd(dmit)_2]_2$ shows a stable superconducting state with $T_c \sim 4.5$ K [31,32,46-49]. Thus, this material is an ideal playground to study correlated superconductivity on a triangular lattice. In addition, the superconductivity of this material looks peculiar because it is adjacent to the VBS state (Fig. 1.4(b)) [32,47], which contrasts with most other correlated superconductors in which the superconducting phase borders a magnetically ordered phase. Thus, the properties of superconductivity in $EtMe_3P[Pd(dmit)_2]_2$ are intriguing and need to be elucidated. In this study, I performed ac susceptibility measurements of $EtMe_3P[Pd(dmit)_2]_2$ under pressure and report the dimensionality of the superconductivity.

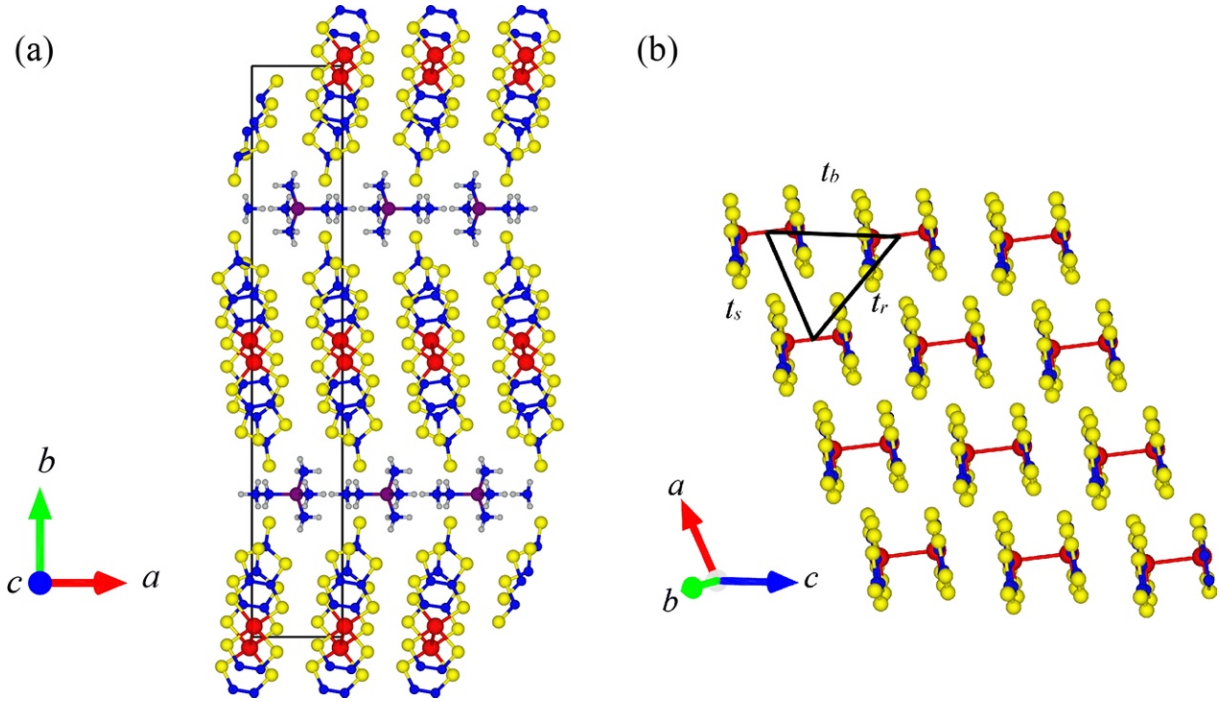

Fig. 2.2. (a) The structure $EtMe_3P[Pd(dmit)_2]_2$. (b) The top view of the $Pd(dmit)_2$ layer of $EtMe_3P[Pd(dmit)_2]_2$. t_b, t_s, and t_r are transfer integral between $Pd(dmit)_2$ dimers. t_b = 28.0, t_s = 27.5, t_r = 29.1 meV [46].

2.1.2 Layered superconductors

Layered superconductors have been intensively studied in the field of physics of quasi-two-dimensional correlated electron superconductivity. These layered superconductors are classified into two categories according to the ratio of the interlayer coherence length $\xi_\perp$ to the layer distance d. If d is sufficiently shorter than $\xi_\perp$ ($\xi_\perp >> d$), the system is regarded as an "anisotropic three-dimensional superconductor (A3DSC)," which can be described by the anisotropic Ginzburg–Landau (GL) model [50]. If d is sufficiently longer than $\xi_\perp$ ($\xi_\perp << d$), the system is regarded as a "two-dimensional superconductor (2DSC)," that is, a set of weakly coupled discrete two-dimensional superconducting layers. A description of the 2DSC requires the Lawrence–Doniach (LD) model [51], in which the discrete layers are weakly coupled through Josephson terms.

All layered superconductors are A3DSCs around the transition temperature T_c under zero magnetic field because $\xi_\perp$ diverges at the transition temperature. Since $\xi_\perp$ decreases on cooling, layered superconductors can undergo a crossover from an A3DSC to a 2DSC at the temperature T^*, where $\xi_\perp$ becomes roughly shorter than d. (To be exact, T^* is defined as the temperature where $\xi_\perp$ reaches $d/\sqrt{2}$ [52,53]). Most of the layered superconductors, such as cuprate superconductors and the representative organic superconductors κ-$(ET)_2X$, undergo the dimensional crossover and show 2DSC natures at low temperatures. For example, the crossover temperature in $Bi_2Sr_2CaCu_2O_{8+x}$ is estimated to be $0.99T_c$ – $0.999T_c$ [50,53–55]. In $YBa_2Cu_3O_{7-\delta}$, which has a relatively strong three-dimensionality among the cuprates, the crossover temperature is estimated to be $0.8T_c$ – $0.9T_c$ [50,53,56,57]. In κ-$(ET)_2Cu[N(CN)_2]Br$, it is estimated to be $0.75T_c$ – $0.97T_c$ [58,59]. The number of layered superconductors that are A3DSCs at temperatures well below T_c is limited.

2.2 Experiment

2.2.1 Samples

I used three fine single crystals of $EtMe_3P[Pd(dmit)_2]_2$. The crystals are plate-like with a typical area of ~1 mm^2 (in the conducting *ac* plane) and a typical thickness of ~50 μm (along the *b*-axis). These crystals were grown using an aerial oxidation method and provided by Prof. R. Kato (RIKEN).

2.2.2 Applying pressure

I packed the single crystal, which is inserted into a coil, into a Teflon capsule filled with a pressure medium (Daphne 7373 oil). I applied pressure of ~5.0 kbar at room temperature with a BeCu clamp cell (Fig. 2.3). The pressure was estimated from the external force applied at room temperature. Note that the applied pressures decrease by 1.5 to 2 kbar upon cooling from room temperature to the oil solidification temperature (200 to 250 K) [60]. The pressure values for the results shown in this paper are those at room temperature.

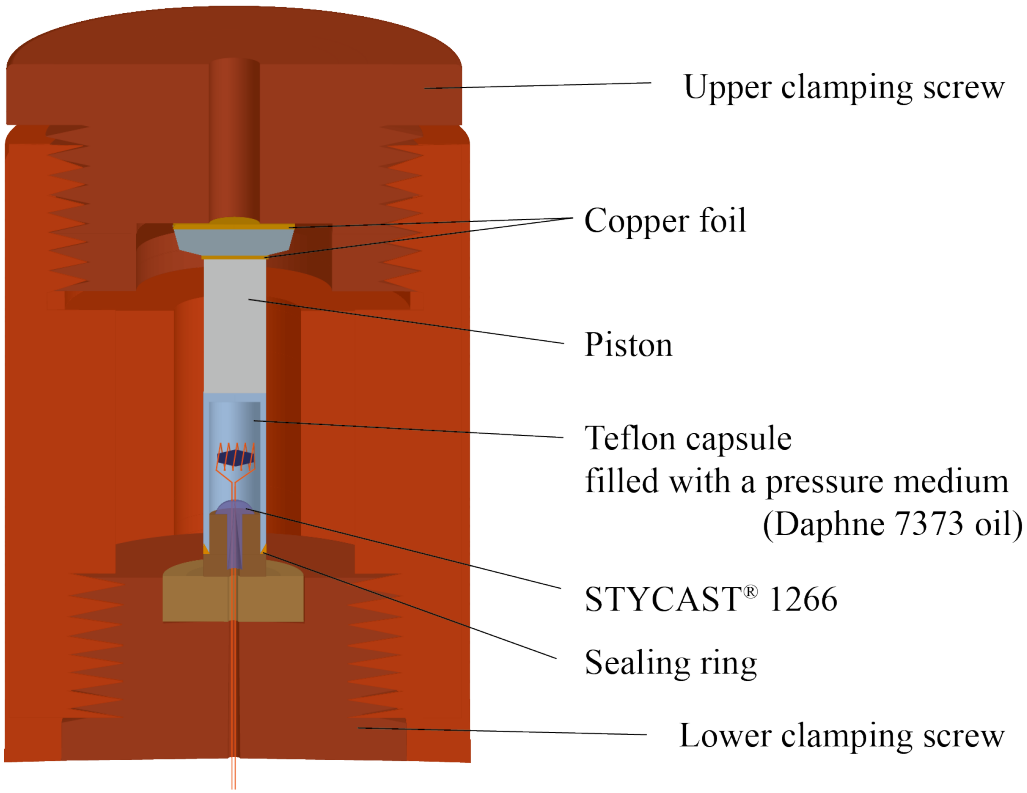

Fig. 2.3. Schematic image of the pressure cell.

2.2.3 AC susceptibility measurement

I measured the ac susceptibility under pressure for single crystals with a dc magnetic field, H_{dc}, applied perpendicular to the ac field, H_{ac}. I inserted a single crystal into the coil, which typically has 125 turns and a dimension ~1 mm × 0.5 mm × 2 mm. The ac susceptibility measurements were performed for three single crystals (No. 1, No. 2, and No. 3) and the results showed good reproducibility for all three crystals. Note that the upper critical field, which is applied perpendicular to the layers, was measured only for the No. 3 sample.

To estimate the ac susceptibility, I measured the resonance frequency f of the LC tank circuit shown in Fig. 2.4(a) using a network analyzer (Agilent Technologies E5061A). The ac field H_{ac} is produced by the ac electric current generated by the network analyzer and flowing through the coil. It was applied nearly parallel to the conducting *ac* layers. Because the samples are sufficiently thin (a typical area of ~1 mm^2 and a typical thickness of ~50 μm), the demagnetization factors for H_{ac} are less than 0.1 and thus ignorable. The magnitude of H_{ac} was about 0.8 Gauss, which is much smaller than the parallel lower-critical field $H_{c1}^{\parallel}$ at low temperatures (44 Gauss) [49]. Since the resonance f is proportional to the inverse of the square root of the coil inductance L ($f = 1/2\pi\sqrt{LC} = f_0/\sqrt{1 + 4\pi\eta\chi}$, where C is the reciprocal sum of individual capacitances), the relation between f and the ac susceptibility χ is denoted by

$$-4\pi\chi = \frac{1}{\eta}\left(1 - \frac{f_0^2}{f^2}\right), \tag{2-1}$$

where f_0 is the resonance frequency of the tank circuit when the sample is in the normal state and η is the filling factor that reflects the ratio of the sample volume to the coil volume. In the three measurements made for the three samples, the values of η are 0.027, 0.033, 0.13, and have uncertainties of ±50%.

In addition to H_{ac}, H_{dc} is applied perpendicular to H_{ac} by a superconducting magnet. The angle between the directions of the Pd(dmit)$_2$ layers of EtMe$_3$P[Pd(dmit)$_2$]$_2$ and H_{dc} is defined as θ, as shown in Fig. 2.4(b); $\theta = 0^\circ$ shows that H_{dc} is exactly parallel to the two-dimensional layers. The angle θ was rotated within $\theta = \pm 15^\circ$ with a rotation pitch of 0.18°.

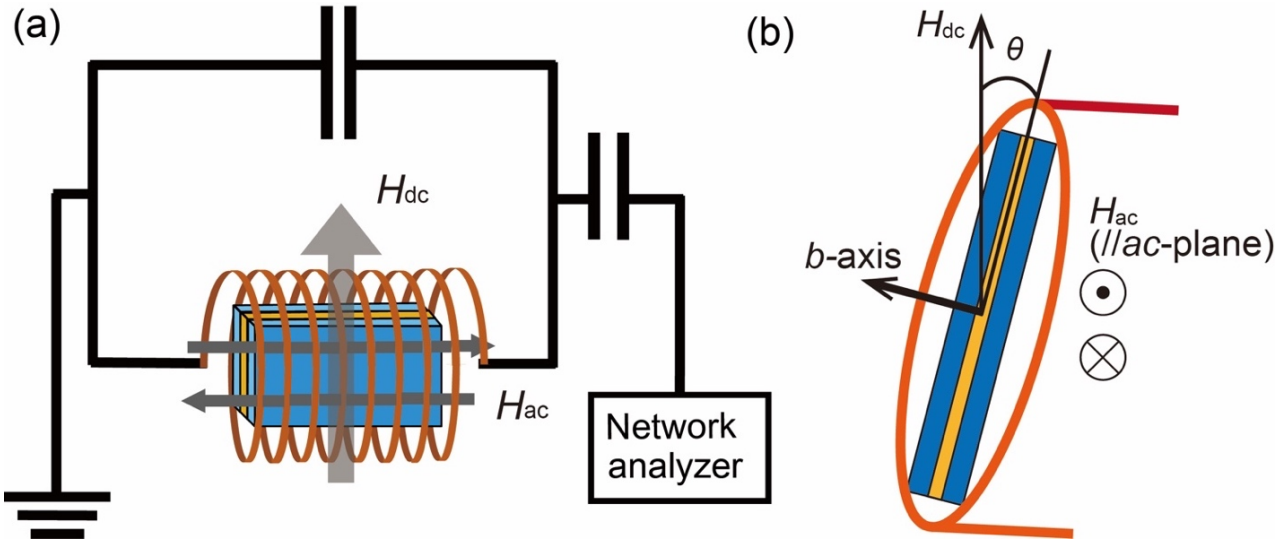

Fig. 2.4. (a) Schematic for the LC tank circuit to measure ac susceptibility. The dc magnetic field H_{dc} was also applied perpendicular to the ac field H_{ac}. (b) Schematic for the configuration of H_{ac} and H_{dc}. The angle between the directions of the Pd(dmit)$_2$ layers and H_{dc} is defined as θ, which was varied by a rotation mechanism.

2.3 Results and Discussion

2.3.1 Diamagnetic signal under H_{dc} = 0 T

Figure 2.5 shows the temperature dependence of the resonance frequency f under H_{dc} = 0 T. The diamagnetic susceptibility due to the Meissner effect is observed as an increase in f. The insets show the temperature dependence of $(1 - f_0^2/f^2)/\eta$, which, as per Eq. (2-1), gives $-4\pi\chi$. Note again that η has uncertainties of ±50%. The volume fraction of the superconductivity, which is estimated from the magnitude of $-4\pi\chi$, is of the order of 100% for all the three samples at the lowest measured temperature, 2.2 K. Although η has considerable uncertainty, this result confirms that the present superconductivity is bulk, which is consistent with the results of the previously reported susceptibility measurements obtained using a superconducting quantum interference device (SQUID) magnetometer [49].

The diamagnetic signal increases rather gradually. One reason is the magnetic penetration effect. Around T_c, the penetration length λ tends to diverge and becomes comparable to or longer than the sample thickness of ~50 μm, which suppresses the diamagnetic signal. However, this effect alone cannot explain the present gradual increase observed in a wide temperature region (observed at least down to ~0.5T_c). Thus, it is natural to think that there is another reason for the gradual increase. The reason is probably that T_c may be distributed to some degree due to possible pressure inhomogeneity or crystal imperfections.

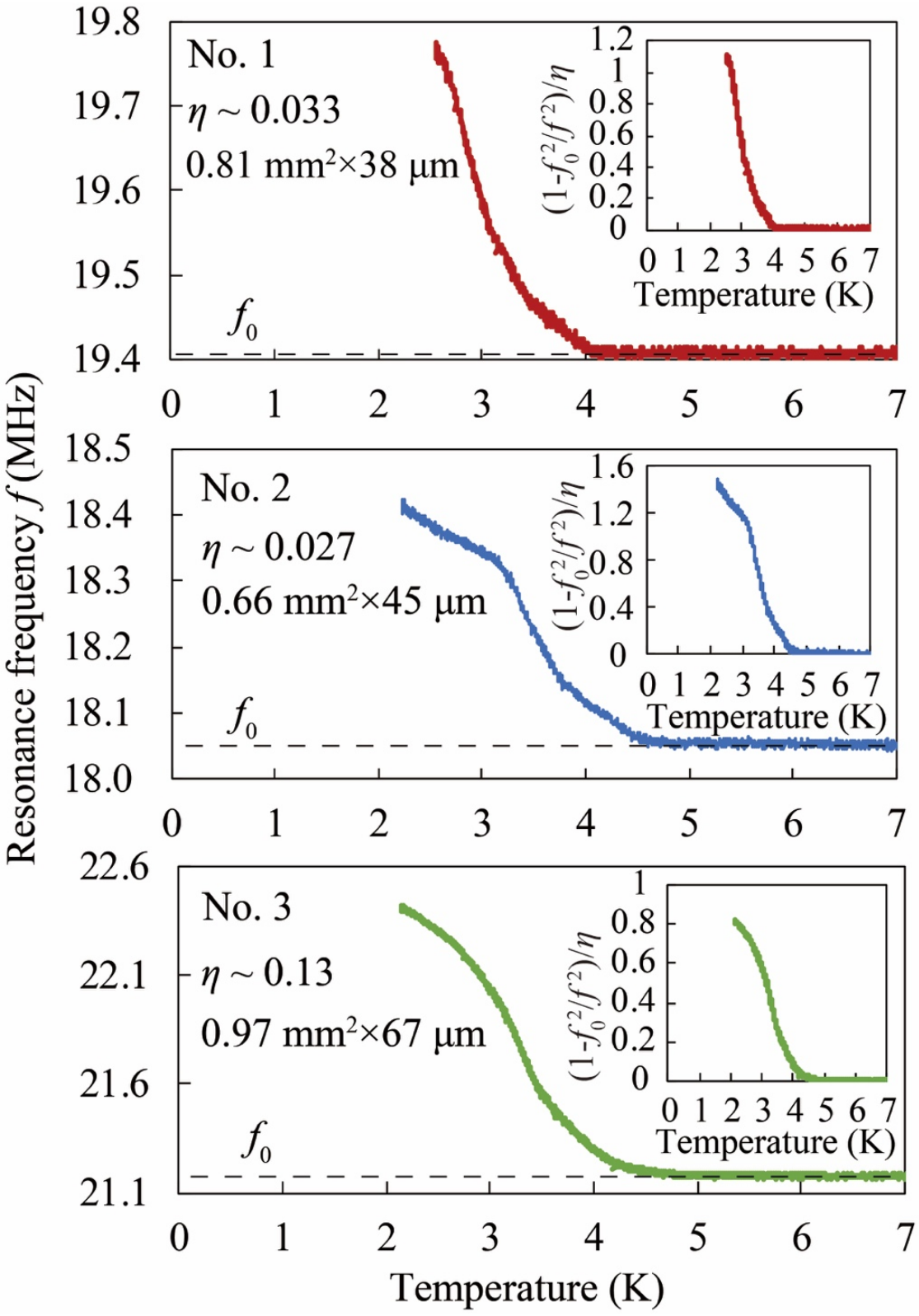

Fig. 2.5. Temperature dependence of the resonance frequency f of the LC tank circuit under $H_{dc} = 0$. The insets show the temperature dependence of $(1 - f_0^2/f^2)/\eta$, where η is ~0.033 for sample No. 1, ~0.027 for sample No. 2, and ~0.13 for sample No. 3. Note that the values of η have uncertainties of ±50%. (This figure is published in Yamamoto *et al*., Phys. Rev. B **97**, 224502 (2018).)

2.3.2 Angle dependence of the diamagnetic signal

Layered 2DSCs generally exhibit the lock-in state with Josephson vortices trapped in insulating layers when H_{dc} is applied nearly parallel to the two-dimensional layers [61], but A3DSCs do not. In other words, whether the lock-in state realizes or does not provide strong information about the dimensionality of superconductivity. When the lock-in state realizes, the ac diamagnetic signal (response to H_{ac} parallel to the two-dimensional layers and perpendicular to H_{dc}) is strongly suppressed because the vortices can easily move according to H_{ac} [61]. Therefore, the ac diamagnetic signal has a characteristic dependence on the angle between the directions of the two-dimensional layers and H_{dc}, showing a strong depression where they are parallel to each other.

As explained in the subsect. 2.2.3, I performed ac susceptibility measurements under H_{dc} applied perpendicular to the ac field H_{ac}. The three samples that I measured show reproducible results, and hereinafter I show data obtained for sample No. 3.

Figure 2.6(a) shows the temperature dependence of $1 - f_0^2/f^2$ at various θ under H_{dc} = 0.025 T and 0.10 T. Figures 2.6(b-e) show the angle dependence of $1 - f_0^2/f^2$ ($\propto -4\pi\chi$) at various temperatures, derived from the data in Fig. 2.6(a). The angle dependence of $1 - f_0^2/f^2$ at each temperature below T_c under ideal conditions [(i) H_{ac} is applied exactly parallel to the conducting *ac* layers of the material and (ii) the rotational axis is exactly parallel to the conducting *ac* layers and perpendicular to the direction of H_{dc}] should be symmetric with respect to the positive and negative values of θ when the superconducting state preserves both the time-reversal symmetry and the mirror symmetry about the *ac* plane. By contrast, in the case that either or both of the experimental conditions (i) and (ii) are not satisfied, the angle dependence of $1 - f_0^2/f^2$ may be asymmetric. This is the possible reason for the observed asymmetric behavior in the angle dependence of $1 - f_0^2/f^2$ (see Figs. 2.6(c-e)). Note that there may be other extrinsic reasons for the asymmetry, such as the effect of the slight stray capacitance of the tank circuit, which may show an unpredictable behavior with respect to θ and thus I cannot conclude the exact reason for the asymmetry in the present situation.

The angle dependence shows no depression around $\theta = 0^\circ$ until 2.25 K, which indicates that the lock-in state is not observed in this experimental condition (see Fig. 2.6). For the representative organic two-dimensional superconductor κ-$(ET)_2Cu(NCS)_2$, the lock-in angle is reported to be within ±10° under 0.1 T and within ±30° under 0.02 T [61]. Indeed, the lock-in angle in the present material for H_{dc} = 0.1 T and 0.025 T is roughly estimated to be within ±1.7° and ±7.0°, respectively, by assuming the rough lock-in condition [$H_{dc}\cdot\sin\theta < H_{c1}^{\perp}$], and the reported value of the lower critical field when the dc field is applied perpendicular to the two-dimensional layers, $H_{c1}^{\perp}$, of $EtMe_3P[Pd(dmit)_2]_2$, $H_{c1}^{\perp}$ = 0.003 T [49]. This estimation is naive; the true values of the lock-in angle may be smaller than the

estimated values. However, the estimated values (in particular, for H_{dc} = 0.025 T, within ±7.0°) are much larger than the present experimental rotation pitch of 0.18°. Thus, the angular resolution is sufficient to detect the lock-in state if it exists. Therefore, I can assert that the superconductivity in $EtMe_3P[Pd(dmit)_2]_2$ never realizes the lock-in state from T_c to 2.25 K. This clearly suggests that the present superconductor does not undergo the crossover to a 2DSC and is an A3DSC even at temperatures much lower than T_c (even at $0.5T_c$).

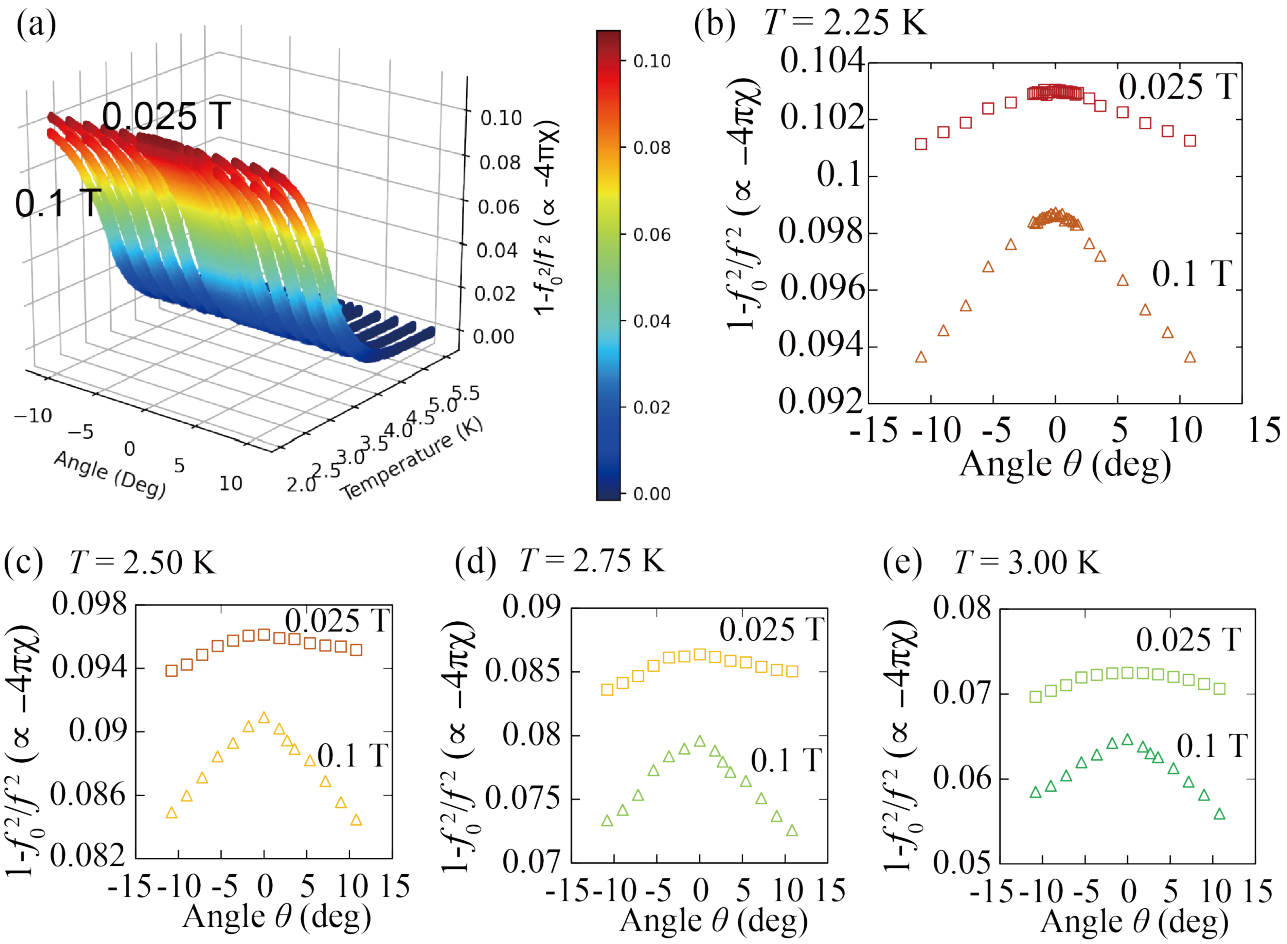

Fig. 2.6. (a) Temperature dependence of $1 - f_0^2/f^2$ at various angles θ under H_{dc} = 0.025 and 0.1 T. (b-e) Angle dependence of $1 - f_0^2/f^2$ under H_{dc} = 0.025 T(squares) and 0.1 T (triangles), derived from the data in Fig. 2.6(a). (This figure is published in Yamamoto *et al.*, Phys. Rev. B **97**, 224502 (2018).)

2.3.3 Temperature dependence of the upper critical fields

When H_{dc} is applied parallel and perpendicular to the two-dimensional layers of a layered superconductor, the upper critical fields just below T_{c0}, which is the transition temperature at $H_{dc} = 0$, are written as

$$H_{c2}^{\parallel}(T) = \frac{\phi_0}{2\pi\xi_{\parallel}(T)\xi_{\perp}(T)} \propto T_{c0} - T, \tag{2-2}$$

$$H_{c2}^{\perp}(T) = \frac{\phi_0}{2\pi\xi_{\parallel}^2(T)} \propto T_{c0} - T, \tag{2-3}$$

where ϕ_0 is the flux quantum, and $\xi_{\parallel}$ ($\xi_{\perp}$) is the intralayer (interlayer) coherence length. Note that the coherence lengths show the temperature dependence, $\xi_{\parallel}(T), \xi_{\perp}(T) \propto (T_{c0} - T)^{1/2}$. Using these equations [Eqs. (2-2), (2-3)], the coherence lengths $\xi_{\parallel}(0)$, $\xi_{\perp}(0)$, which reflect the coherence length at absolute zero temperature (the Pippard length), can be obtained from the measured $H_{c2}^{\parallel}(T)$ and $H_{c2}^{\perp}(T)$. Because these equations [Eqs. (2-2), (2-3)] are only valid just below T_{c0}, they can be rewritten as

$$-T_{c0} \left.\frac{dH_{c2}^{\parallel}(T)}{dT}\right|_{T=T_{c0}} = \frac{\phi_0}{2\pi\xi_{\parallel}(0)\xi_{\perp}(0)}, \tag{2-4}$$

$$-T_{c0} \left.\frac{dH_{c2}^{\perp}(T)}{dT}\right|_{T=T_{c0}} = \frac{\phi_0}{2\pi\xi_{\parallel}^2(0)}. \tag{2-5}$$

Thus, the data on $H_{c2}^{\parallel}(T)$ and $H_{c2}^{\perp}(T)$ just below T_{c0} give information on the coherence lengths, giving additional supportive insight into the dimensionality of the superconductivity.

As explained in the subsect. 2.2.3, I performed ac susceptibility measurements under H_{dc}. I fixed the direction of H_{dc} to be $\theta = 0^{\circ}$ (parallel to the layers), 90° (perpendicular to the layers) and obtained $1 - f_0^2/f^2$ under several values of H_{dc}. Figures 2.7(a), 2.8(a) show the temperature dependence of $1 - f_0^2/f^2$ at $\theta = 0^{\circ}$, 90° under various H_{dc}. Figures 2.7(b), 2.8(b) show the temperature dependence of $H_{c2}^{\parallel}(T)$ and $H_{c2}^{\perp}(T)$ obtained by the arrows in Figs. 2.7(a), 2.8(a). The upper critical fields were extracted from the crossing point between linear extrapolation lines of $1 - f_0^2/f^2$ and the baseline. To discuss the uncertainty in $H_{c2}^{\parallel}(T)$ and $H_{c2}^{\perp}(T)$, I performed the linear extrapolation in three different regions, $0.005 < 1 - f_0^2/f^2 < 0.01$, $0.01 < 1 - f_0^2/f^2 < 0.02$, and $0.02 < 1 - f_0^2/f^2 < 0.03$ for $H_{c2}^{\parallel}(T)$, and $0.001 < 1 - f_0^2/f^2 < 0.002$, $0.002 < 1 - f_0^2/f^2 < 0.006$, and $0.006 < 1 - f_0^2/f^2 < 0.01$ for $H_{c2}^{\perp}(T)$, as shown in Figs. 2.7(a), 2.8(a). The initial values of the gradient of $H_{c2}^{\parallel}$ ($dH_{c2}^{\parallel}/dT$ around T_c) are -2.7 ± 0.2 T/K and those of $H_{c2}^{\perp}$ ($dH_{c2}^{\perp}/dT$ around T_c) are -0.33 ± 0.5 T/K.

Thus, the coherence lengths $\xi_{\parallel}(0)$ and $\xi_{\perp}(0)$ are estimated to be 145±20 Å and 21±5 Å, respectively. Thus, the interlayer coherence length $\xi_{\perp}$ is comparable to or longer than the layer distance d of $EtMe_3P[Pd(dmit)_2]_2$ (18 Å). This is consistent with the previously discussed conclusion that $EtMe_3P[Pd(dmit)_2]_2$ under pressure is an A3DSC.

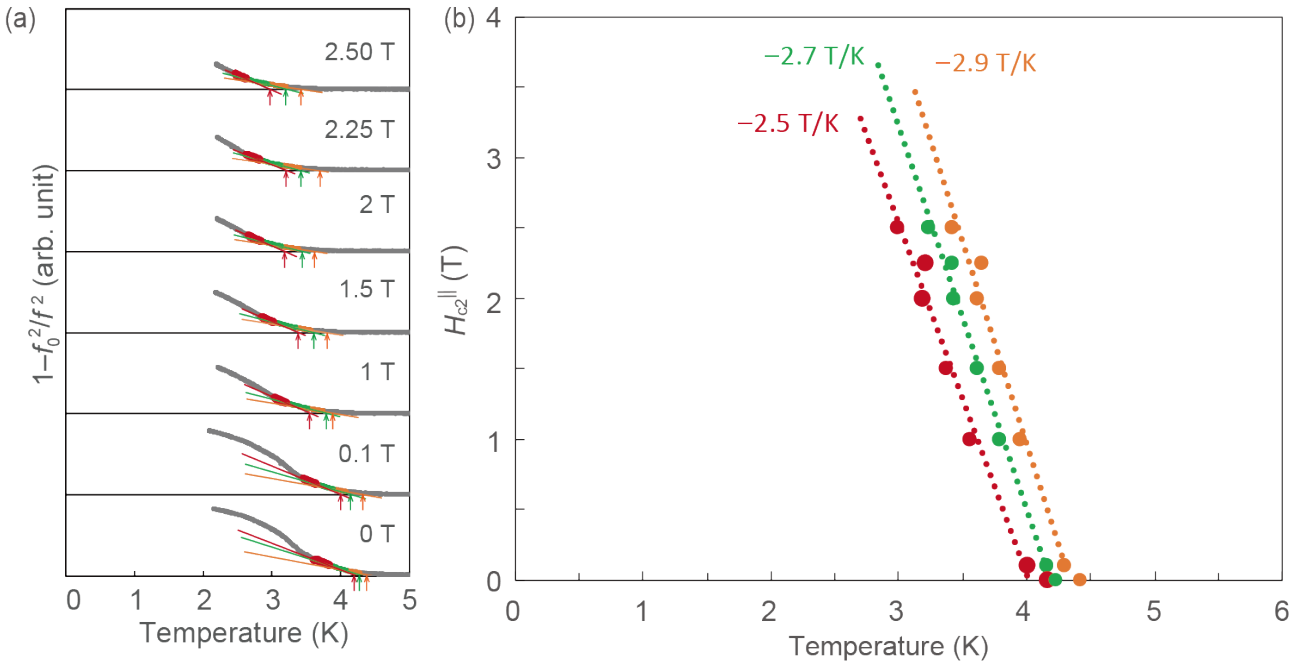

Fig. 2.7. (a) Temperature dependence of $1 - f_0^2/f^2$ at $\theta = 0^\circ$ under various H_{dc}. (b) Temperature dependence of $H_{c2}^{\parallel}(T)$ obtained by the arrows in Fig. 2.7(a). The data with orange, green, and yellow colors in Fig. 2.7(b) are obtained by the arrows with the same color in Fig. 2.7(a).

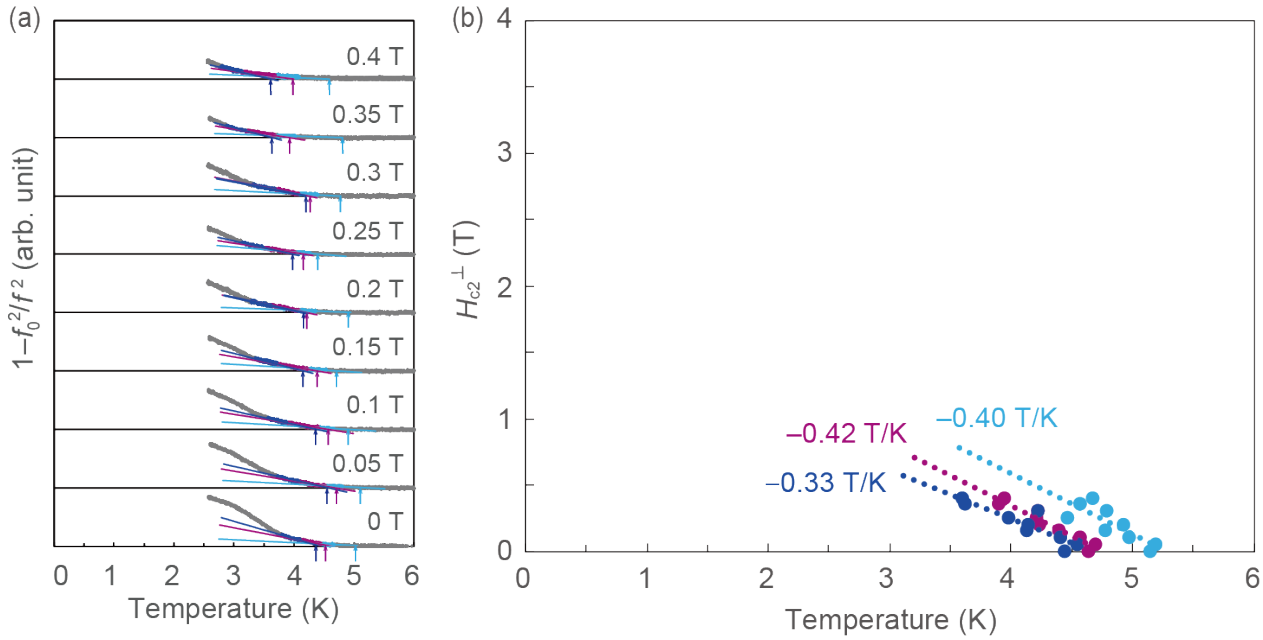

Fig. 2.8. (a) Temperature dependence of $1 - f_0^2/f^2$ at $\theta = 90^\circ$ under various H_{dc}. (b) Temperature dependence of $H_{c2}^{\perp}$ obtained by the arrows in Fig. 2.8(a). The data with light blue, purple, and dark blue colors in Fig. 2.8(b) are obtained by the arrows with the same colors in Fig. 2.8(a).

2.3.4 Angle dependence of the transition temperature

The angle dependencies of the upper critical field $H_{c2}(\theta)$ for 2DSCs and A3DSCs are distinguishable; thus, $H_{c2}(\theta)$ gives supporting information on the dimensionality of superconductivity.

For 2DSCs, the Tinkham model gives the following relation of $H_{c2}(\theta)$ [50, 62]:

$$\left|\frac{H_{c2}(\theta)\sin\theta}{H_{c2}^{\perp}}\right| + \left(\frac{H_{c2}(\theta)\cos\theta}{H_{c2}^{\parallel}}\right)^2 = 1. \tag{2-6}$$

Note that the angle dependence of $H_{c2}(\theta)$ for 2DSCs shows a cusp at $\theta = 0^{\circ}$. For A3DSCs, according to the anisotropic GL model, $H_{c2}(\theta)$ satisfies the following relation [50,51]:

$$\left(\frac{H_{c2}(\theta)\sin\theta}{H_{c2}^{\perp}}\right)^2 + \left(\frac{H_{c2}(\theta)\cos\theta}{H_{c2}^{\parallel}}\right)^2 = 1. \tag{2-7}$$

In contrast to 2DSCs, the angle dependence of $H_{c2}(\theta)$ for A3DSCs shows smooth behavior at $\theta = 0^{\circ}$ without a cusp. The singularity in the angle dependence of the transition temperature T_c is essentially the same as that in $H_{c2}(\theta)$ because

$$\frac{\partial T_c(H_{dc},\theta)}{\partial\theta} = \frac{\partial T_c(H_{dc},\theta)}{\partial H}\left(\frac{dH_{c2}(\theta)}{d\theta}\right)_{T=T_c}, \tag{2-8}$$

and

$$\frac{\partial T_c(H_{dc},\theta)}{\partial H_{dc}} \neq 0.$$

Accordingly, the angle dependence of T_c shows a cusp at $\theta = 0^{\circ}$ in 2DSCs and no cusp in A3DSCs.

Indeed, according to Welp *et al.* [56], the angle dependencies of T_c under H_{dc} for 2DSCs and A3DSCs satisfy the following relations, which show a cusp and smooth behavior, respectively. For 2DSCs,

$$T_c(H_{dc},\theta) = T_{c0} - |\{T_{c0} - T_c^{\perp}(H_{dc})\}\sin\theta| - \left\{T_{c0} - T_c^{\parallel}(H_{dc})\right\}\cos^2\theta, \tag{2-9}$$

where $T_c^{\perp}(H_{dc})$ and $T_c^{\parallel}(H_{dc})$ are the transition temperature when H_{dc} is applied perpendicular and parallel to the conducting layers, respectively. For A3DSCs,

$$T_c(H_{dc},\theta) = T_{c0} + \frac{H_{dc}}{dH_{c2}^{\parallel}(T)/dT}\left(\cos^2\theta + \frac{m^{\perp}}{m^{\parallel}}\sin^2\theta\right)^{1/2}, \tag{2-10}$$

where $m^{\perp}/m^{\parallel} = (\xi_{\parallel}/\xi_{\perp})^2$ is an anisotropic factor of A3DSCs.

Figure 2.9(a) shows the temperature dependence of $1 - f_0^2/f^2$ at various angles under H_{dc} = 1.00 T. Figure 2.9(b) shows the angle dependences of T_c obtained by the arrows in Fig. 2.9(a). The superconducting transition temperatures were determined in the same way as the method for determining $H_{c2}^{\parallel}(T)$ and $H_{c2}^{\perp}(T)$ described in the subsect. 2.3.3. The three regions in which I performed the linear extrapolation are $0.005 < 1 - f_0^2/f^2 < 0.01$, $0.01 < 1 - f_0^2/f^2 < 0.02$, and 0.02

$< 1 - f_0^2/f^2 <$ 0.03, as shown in Fig. 2.9(a). As seen in Fig. 2.9(b), the angle dependences of T_c (which is approximately 3.9 K, 3.7 K, and 3.5 K at $\theta = 0^\circ$) do not show a cusp but show smooth behavior around $\theta = 0^\circ$. Besides, it is well fitted by the model for A3DSC [Eq. (2-10)] while it is not fitted by the model for 2DSC [Eq. (2-9)].

In this model for A3DSC fitting, T_{c0} and $m^\perp/m^\parallel$ are treated as fitting parameters, and $dH_{c2}^{\parallel}/dT$ is set to be a constant value, −2.7 T/K, which is obtained in the subsect. 2.3.3. The best fittings shown in the solid line in Fig. 2.9(b) give T_{c0} = 4.1±0.2 K and $m^\perp/m^\parallel$ = 45±9. To check the reliability of these fittings by the model for A3DSC, I compared the experimentally obtained values of T_{c0} and $m^\perp/m^\parallel = (\xi_\parallel/\xi_\perp)^2$ with the values obtained by the fittings. The experimentally obtained value of T_{c0} is 4.1±0.3 K and of $m^\perp/m^\parallel$ is 50±15. This is well consistent with the obtained values by the fitting. Therefore, this result also gives supporting evidence for the conclusion that $EtMe_3P[Pd(dmit)_2]_2$ under pressure is an A3DSC (at least around 3.9 K).

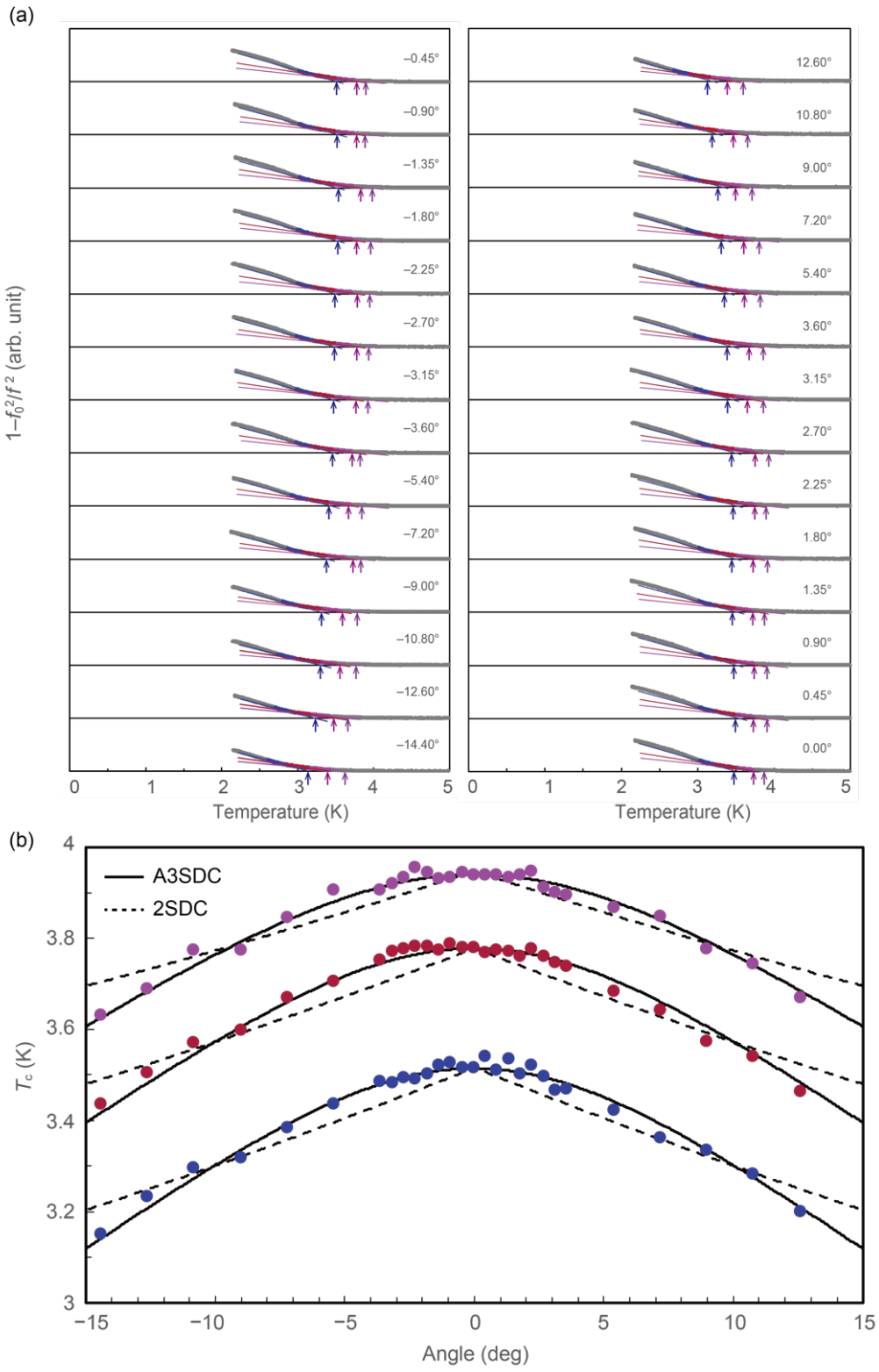

Fig. 2.9. (a) Temperature dependence of $1 - f_0^2/f^2$ at various angles θ under $H_{dc} = 1.00$ T. (b) Angle dependence of the transition temperature, T_c, obtained by the arrows in Fig. 2.9(a). The data with purple, red, and dark blue colors in Fig. 2.9(b) are obtained by the arrows with the same colors in Fig. 2.9(a). The solid and dashed lines are the fitted curves of the models for A3DSC and 2DSC, respectively. The model for A3DSC can fit the data very well, while the model for 2DSC cannot.

2.3.5 The molecular orbital

As discussed previously, I concluded that the superconductivity in $EtMe_3P[Pd(dmit)_2]_2$ under pressure is an A3DSC even at low temperatures, which is in striking contrast to the large majority of other correlated electron layered superconductors such as cuprates and κ-$(ET)_2X$ systems. Indeed, the intralayer coherence lengths $\xi_{\parallel}$ in $EtMe_3P[Pd(dmit)_2]_2$ and that in κ-$(ET)_2Cu_2(CN)_3$ are almost identical, but the interlayer coherence length $\xi_{\perp}$ in $EtMe_3P[Pd(dmit)_2]_2$ is about twice as long as that in κ-$(ET)_2Cu_2(CN)_3$ [63] (Table 2.1). Note that κ-$(ET)_2Cu_2(CN)_3$ is also the nearly isotropic triangular lattice system with almost the same transfer integrals [64–66] and electron correlation energies [65,66] as those in $EtMe_3P[Pd(dmit)_2]_2$ and has T_c (= 3.8 K [67,68]) near that in $EtMe_3P[Pd(dmit)_2]_2$.

The possible reason for the realization of this superconductivity in $EtMe_3P[Pd(dmit)_2]_2$ is the molecular orbital in terminal atoms. In the ET molecule, the terminal atoms are hydrogen (see, Fig. 1.3(a)), and the molecular orbital density on the hydrogen atoms of ET at the Fermi energy is negligibly small [69]. Because the orbital overlap between the terminal atoms causes the interlayer coupling, the coupling in the κ-$(ET)_2X$ systems is expected to be weak. On the other hand, in the $Pd(dmit)_2$ molecule, the terminal atoms are sulfur (see, Fig. 1.3(b)), and the molecular orbital density of $Pd(dmit)_2$ at the Fermi energy is spread to these sulfur atoms [70,71]. Besides, the smallest interlayer S−S distance in $EtMe_3P[Pd(dmit)_2]_2$ (3.6753 Å) is especially short among the $Y[Pd(dmit)_2]_2$ systems. Note that a recent work of Shimizu *et al*. [72], which discussed the anisotropy of the resistivity, proposed a three-dimensional nature in the normal phase of this material; the authors also expected that the interlayer S−S distance relates to the dimensionality [72]. Hence the coupling in $EtMe_3P[Pd(dmit)_2]_2$ is expected to be strong. This probably causes the present peculiar superconductivity in $EtMe_3P[Pd(dmit)_2]_2$.

Table 2.1. Coherence lengths and layer distance

Material	$\xi_{\parallel}$ [Å]	$\xi_{\perp}$ [Å]	d [Å]	$\xi_{\perp}(0) / d$
κ-$(ET)_2Cu_2(CN)_3$ [63]	110	10	15	0.66
$EtMe_3P[Pd(dmit)_2]_2$	145±20	21±5	18	1.2±0.3

2.4 Conclusion

I have investigated the dimensionality of superconductivity in $EtMe_3P[Pd(dmit)_2]_2$ under pressure by ac susceptibility measurements with the application of the dc magnetic field. I have obtained the following three results: (i) The angle dependence of the ac susceptibility at 2.25 K shows no depression around $\theta = 0^\circ$. This clearly indicates that the lock-in state, which is characteristic of 2DSCs, does not realize in the present system; (ii) The angle dependence of T_c does not show a cusp but shows smooth behavior at $\theta = 0^\circ$; (iii) The value of interlayer coherence length $\xi_\perp$ is longer than the layer distance d of $EtMe_3P[Pd(dmit)_2]_2$. From these results, I concluded that $EtMe_3P[Pd(dmit)_2]_2$ under pressure is an A3DSC even at temperatures much lower than T_c (even at ~0.5 T_c).

3 Electronic Griffiths Phase in x-ray irradiated κ-$(ET)_2Cu[N(CN)_2]Cl$

3.1 Introduction

3.1.1 Hierarchy of energy and length scales in physics

Science has been studied in different ways, classified into many academic subfields that are characterized by the characteristic length scales and energy scales of observation objects. Even within physics, there are several subfields. The relationship between particle physics and solid-state physics can be understood by the difference in the scales (Fig. 3.1). For example, as for the object is quarks and/or leptons, the characteristic length scale is ~10^{-18} m, which is dominated by the range of the weak nuclear force, and the energy scale is ~10^{12} eV; the corresponding subfield in physics is particle physics. For hadrons, the length scale is ~10^{-15} m, which is dominated by the range of the strong nuclear force, and the energy scale is ~10^{9} eV; the subfield is nuclear physics. For atoms, molecules, and crystals, the length scales are 10^{-10} ~ 10^{-9} m, which corresponds to the size of the atoms and the unit cell of the crystals, and the energy scale is ~10^{0} eV; the subfield is solid-state physics, which I have studied. It is noteworthy that a hadron is composed of quarks, and an atom, a molecule, and a crystal are composed of many hadrons and electrons (leptons). They are related to each other but produce different physics; for example, when we discuss physical properties of a crystal, we use solid-state physics, but there is no need to deal with them from the viewpoints of particle physics and/or nuclear physics. This fact suggests the existence of a hierarchy of these scales in physics and that each physics subfield represents each level of the hierarchy.

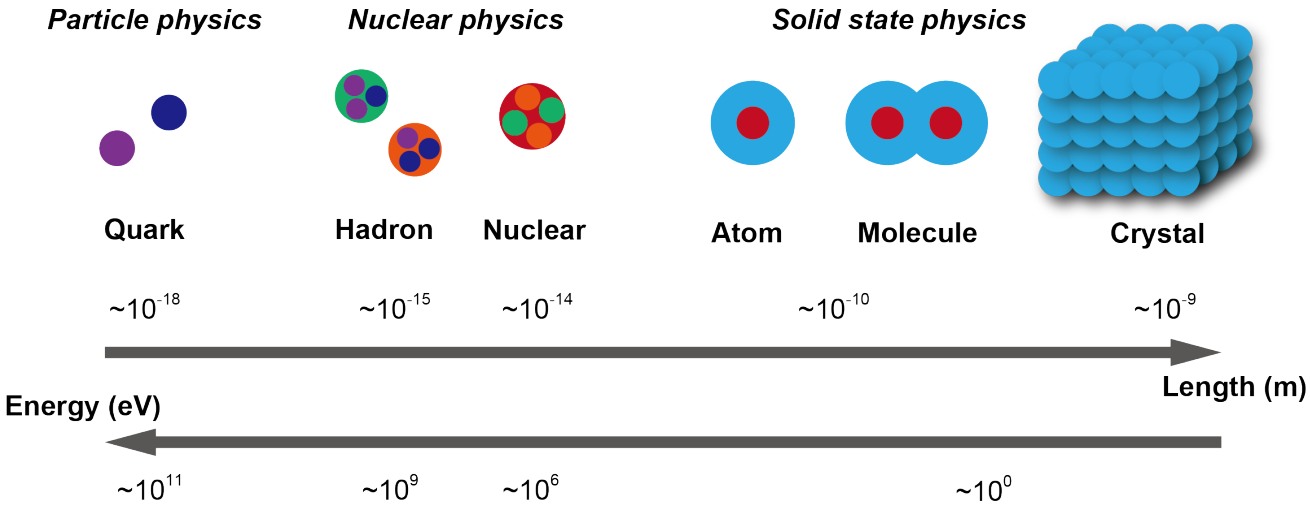

Fig. 3.1. The relationship between particle physics and solid-state physics.

Electron dynamics in solid matters is described by an electronic Hamiltonian, regardless of whether the dynamics is dominated by single electrons or by collective excitations. The Hamiltonian generally contains transfer integrals and/or Coulomb repulsions, all of which are ~10^0eV as explained above, and reside in the THz region (To be exact, 1 THz correspond to 4.14 meV and I called the region between ~10^0 THz and ~10^3 THz "the THz region"). This has led to the general consensus that the electron dynamics has a structure in the THz region, which is characterized by the energy scale of ~10^0eV and is frequency-independent below the THz region. However, in the long history of solid-state physics, exceptions have been found: the dynamics of superconducting vortices [73], incommensurate charge-density waves [74], and domain walls between different phases [75,76]. They are all characterized by a long-range order of the electronic states and consequently have a length scale much longer than the atomic distance scale. This straightforwardly produces a new frequency-scale that is much slower than the energy scale of the original Hamiltonian (in solid-state physics), according to the length scale – energy scale correspondence as explained above. Recently, some correlated electron systems, such as high-T_c cuprates [77-86] and manganites [87-94], have been found to show long-length self-organization in their electronic structures but without long-range order, which is also accompanied by extraordinarily slow dynamics [95]. These features are rather similar to phenomena observed in "structured fluids [96]" in soft-matter systems and suggest the emergence of a new hierarchical level.

3.1.2 Purpose and κ-$(ET)_2Cu[N(CN)_2]Cl$

I have thought and some theoretical researchers [95,97] pointed out that the key in approaching the emergence of a new hierarchical level is probably the synergistic effect between the effects of strong electron correlation and randomness, because high-T_c cuprates and manganites have both effects. However, few systematic experimental studies of this issue have been conducted, because independent control of electron correlation and randomness is difficult in these materials; In the previous studies using these materials, the introduction of randomness is not appropriate because it is done by site substitutions, which also affected the symmetry and/or lattice parameters of the crystal. Recently, Itou *et al.* reported that such slow dynamics have also been observed in a correlated-electron organic system [98]. The authors compared the electron dynamics in two organic materials with different space groups (ground states); and thus, they found that only one of them, the one with randomness in the crystal structure, displays the slow dynamics, while the other, the one that has no randomness, does not. Based on this observation, they proposed that the slow dynamics may be also caused by the interplay between the effects of electron correlation and randomness. However, this suggestion is inconclusive, because the randomness was not controlled in an identical material.

To investigate the present issue, the bandwidth-controlled Mott-transition systems κ-$(ET)_2X$ are appropriate, because we can independently control electron correlation and randomness in an identical material by applying pressure and x-ray irradiation, respectively [99]. In particular, x-ray irradiation to the antiferromagnetic Mott insulator κ-$(ET)_2Cu[N(CN)_2]Cl$ (hereinafter abbreviated as κCl, the Néel temperature T_N = 23 K [18,100]; Figs. 3.2(a,b)) has recently been receiving considerable attention. In κCl, the ET layer, which forms a quasi-two-dimensional electronic system, is segregated by a nonmagnetic insulating anion layer $Cu[N(CN)_2]Cl^-$. The ET dimer plays the role of one lattice point of an anisotropic triangular lattice, and an effective single-band Hubbard Hamiltonian with on-site Coulomb repulsion and transfer integrals between the ET dimers can describe the fundamental properties of the system [17]. X-ray irradiation directly induces defects of the C−N bonds in the anion layers [99,101], and a first-principles calculation suggests that the defects are the local rearrangements of the C−N bonds [102]. It is believed that the defects of the C−N bonds cause a random modulation mainly of the local potential in the conducting ET layers. Further, applying pressure increases the bandwidth and thus can control the magnitude of electron correlation. Nonirradiated κCl is near the Mott boundary, which separates the Mott insulator and the Fermi liquid state with a critical endpoint as described in the subsect. 1.1.3; the Mott transition is realized under very weak pressure, $P_c \sim 0.25$ kbar [21,22,30]. Note that the change of the physical properties caused by the randomness produced by x-ray irradiation is nontrivially enhanced particularly for the κ-$(ET)_2X$ system near the Mott

boundary even though the amount of randomness is slight [99]. For the charge degrees of freedom, x-ray irradiation of κCl for 500-h suppresses the resistivity at low temperatures by four orders of magnitude, though the temperature dependence of the resistivity still shows a weak insulating behavior (Fig. 3.2(c)). For the spin degrees of freedom, the irradiation extinguishes the antiferromagnetic long-range order ((Fig. 3.2(d)), which was observed by ^{1}H-NMR [103].

To obtain detailed information about the electronic dynamics of 500-h-irradiated κCl (500h-0kbar-κCl), I performed ^{13}C-NMR measurements for a ^{13}C-enriched κCl single crystal irradiated with x-ray for 500 h at ambient pressure and 5 kbar (500h-5kbar-κCl) under an 8.0 T magnetic field. For comparison, I also performed ^{13}C-NMR measurements for a nonirradiated single crystal at ambient pressure (0h-0kbar-κCl) under an 8.0 T magnetic field. Note that ^{1}H-NMR cannot detect the dynamics in detail owing to poor HOMO densities on the H sites [69].

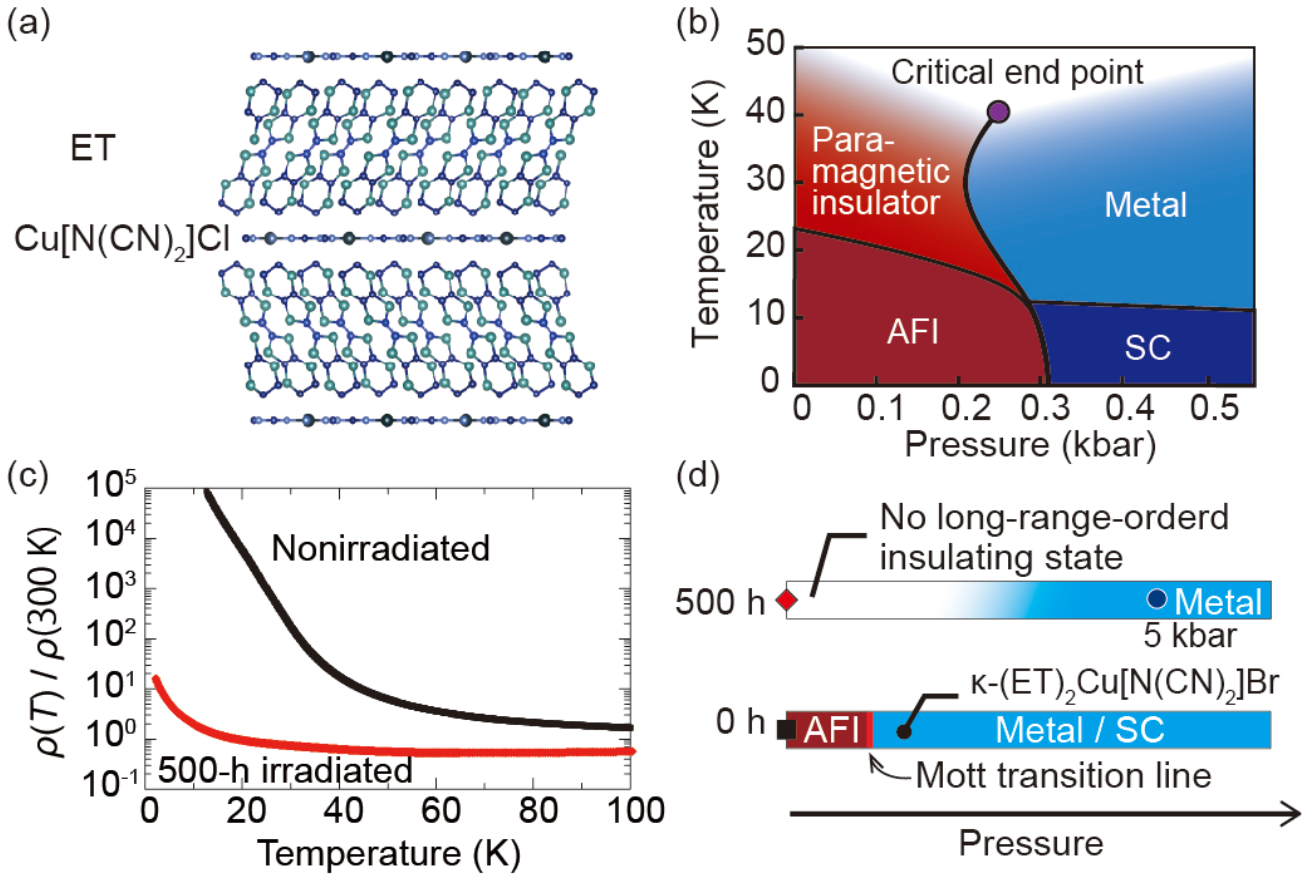

Fig. 3.2. (a) The layered structure of κCl. The defects induced by x-ray irradiation are in the anion layers [99,101] (local rearrangements of the C−N bonds in the anion [102]). (b) Pressure-temperature phase diagram of nonirradiated κCl [21,22]. AFI and SC denote antiferromagnetic ordered insulator and superconductor, respectively. (c) Temperature dependence of the in-plane resistivity of nonirradiated (black line) and 500 h x-ray-irradiated (red line) κCl. The resistivity data have been normalized to the room-temperature value for each sample. The data for the former were obtained in a previous study [103]. (d) Schematic low-temperature phase diagram of non-irradiated (0 h) and 500-h irradiated κ-$(ET)_2X$ (X = $Cu[N(CN)_2]Cl$ and $Cu[N(CN)_2]Br$) as a function of pressure [21,22,103,104]. The black squares, red diamonds, and blue circles represent the 0h-0kbar-κCl, 500h-0kbar-κCl, and 500h-5kbar-κCl samples, respectively. (This figure is published in Yamamoto *et al.*, Phys. Rev. Lett. **124**, 046404 (2020).)

3.2 Experiment

3.2.1 Samples

I used single crystals of κCl, in which ^{13}C was enriched for the doubly bonded carbon sites at the center of ET (Fig. 3.3(a)). The dimensions of the measured samples are approximately 0.96 mm × 1.5 mm × 0.23 mm (thickness) for the non-irradiated crystal and 0.82 mm × 0.86 mm × 0.39 mm (thickness) for the 500-h irradiated crystal. These crystals were grown using the conventional electrochemical method and provided by Dr. K. Miyagawa (the University of Tokyo).

3.2.2 X-ray irradiation

One of the measured samples was irradiated with a white X-ray at room temperature using a non-filtered tungsten target at 40 kV and 20 mA. The dose rate was approximately 0.5 MGy / hour. To attain a uniform dose over the sample, I used a sample sufficiently thinner than the X-ray attenuation length, ~1 mm, which has been calculated for the present compound [105], and the sample was irradiated both sides. The total irradiation time was 500 h. This x-ray irradiation was performed by my collaborator Prof. T. Sasaki (Tohoku University).

3.2.3 Applying pressure

For the pressure study, I placed the 500-h irradiated sample to a clamp-type BeCu pressure cell with the pressure medium Daphne 7373 oil, as explained in chapter 2. I applied hydrostatic pressure (5 kbar) at room temperature. Note that the applied pressure decreases by 1.5 to 2 kbar upon cooling from room temperature to the oil solidification temperature (200 to 250 K). The pressure value for the results shown in this chapter is those at room temperature.

3.2.4 NMR

I measured the ^{13}C-NMR spectra, the nuclear spin-lattice relaxation rate T_1^{-1}, and the nuclear spin-spin relaxation rate (the spin-echo decay rate) T_2^{-1} under a magnetic field of approximately 8.0 T applied almost perpendicular to the conducting plane (for details, see the below). I obtained the NMR spectra by Fourier transforming the quadrature-detected echo signals. I used the spin-echo pulse sequences of $\pi/2$–τ–π, where τ is the RF pulse interval time. The widths of the $\pi/2$ and π pulses, respectively, were typically1.5 and 3.0 μsec for 500h-0kbar-κCl, 1.5 and 3.0 μsec for 500h-5kbar-κCl, and 3.0 and 6.0 μsec for 0h-0kbar-κCl. I obtained T_1^{-1} from the recovery of the frequency-integrated Fourier-transformed spin-echo intensity $M(t)$, where t is the time interval between the saturation comb pulses and the $\pi/2$ pulse. I fitted the relaxation curves, $1-M(t)/M(\infty)$ vs. t, using the stretched-exponential function, $\exp\{-(t/T_1)^{\beta}\}$, where β is the stretching exponent. I obtained T_2^{-1} from the decay of the spin-echo intensity $I(2\tau)$ (for details, see the bellow).

3.2.4.1 ^{13}C-NMR spectra

When an external magnetic field is applied to κCl along an arbitrary direction, the ^{13}C-NMR spectra generally consist of 16 (2 × 2 × 4, as explained below) resonance lines. This line splitting is due to the following three reasons: (i) the shifted face-to-face dimerization of the ET molecules makes the two central carbon sites in ET (termed the “inner” and “outer” sites, as depicted in Figs. 3.3(a, b)) inequivalent, producing two lines with different shifts; (ii) each line is further split into two by the nuclear-dipole fields from adjacent ^{13}C nuclei, which is called the “Pake doublet”; (iii) the unit cell contains four dimers (two in a layer) that become inequivalent when a magnetic field is applied along any direction except the highly symmetric directions (see Figs. 3.3(d-f)). Indeed, the measured ^{13}C-NMR spectra at 261 K are decomposed into more than ten lines (Fig. 3.4). I need to know the precise direction of the external magnetic field to perform T_2^{-1} analysis discussed later; below, I determine the field directions by considering the relation between the field directions and the degree of splitting due to effects (i)-(iii) above.

I first consider the resonance lines coming from the ^{13}C nuclei in one dimer. In other words, I focus on the effects (i) and (ii). For the line splitting due to the effect (i), for the i th dimer in the unit cell the shift difference δ_i between the lines from the ^{13}C nuclei at the outer and inner sites is given by

$$\delta_i = \frac{\gamma \boldsymbol{H}_0 \{A_{\mathrm{out},i}(T) - A_{\mathrm{in},i}(T)\} \boldsymbol{H}_0}{|\boldsymbol{H}_0|}, \tag{3-1}$$

where $\boldsymbol{H}_0$ is the applied external magnetic field, $\gamma = 10.7054$ MHz/T is the gyromagnetic ratio of ^{13}C nuclei, and $\boldsymbol{A}_{\mathrm{out},i}(T)$ and $\boldsymbol{A}_{\mathrm{in},i}(T)$ are the shift tensors for the outer and inner sites in the i th dimer in the

unit cell at temperature T. The x-ray irradiation does not damage the ET molecules [99,101,102]; thus, it hardly changes the distribution of the electron density in an ET molecule or the uniform spin susceptibility at high temperatures. Accordingly, it is reasonable to assume that the shift tensor at high temperatures is not altered by the x-ray irradiation. I thus adopt the shift tensors for κ-$(ET)_2Cu[N(CN)]_2Br$ at 295 K reported in Ref. [106] as the matrix elements $\boldsymbol{A}_{\mathrm{out},i}(T)$ and $\boldsymbol{A}_{\mathrm{in},i}(T)$ at high temperatures ($T > 100$ K). [The shift tensors for κ-$(ET)_2Cu[N(CN)]_2Br$ and κCl at high temperatures are most likely to be almost the same.] Hence, the values of δ_i at high temperatures can be determined when the direction of the external magnetic field is given.

For the line splitting due to effect (ii) for i th dimer in the unit cell, the Pake-doublet splitting J_i is given by,

$$J_i = \frac{\gamma^2\hbar}{r^3}(1 - 3\cos^2\psi_i), \tag{3-2}$$

where r = 1.38 Å is the distance between the adjacent ^{13}C nuclei at the center of ET, and ψ_i is the angle between the directions of the double bond between these ^{13}C nuclei and the external magnetic field $\boldsymbol{H}_0$. Thus, I can determine J_i as well as δ_i, given the direction of the external magnetic field. When δ_i and J_i are determined for one dimer in a unit cell—for example δ_1 and J_1—the other three sets of values $\delta_{i=2,3,4}$ and $J_{i=2,3,4}$ are also determined, owing to the space-group symmetry of κCl (P_{nma}). I, therefore, fitted the experimental spectrum for each measurement at high temperature (261 K for 500h-0kbar-κCl, 273 K for 500h-5kbar-κCl, and 98.8 K for 0h-0kbar-κCl) to the simulated lines, using the angles (θ, ϕ) between the external field and the crystal axes (Fig. 3.3(c)) as fitting parameters. [For example, Fig. 3.4 shows a good fit to the data for 500h-0kbar-κCl at T = 261 K, obtained by varying the parameters (θ, ϕ)]. In this way, I found the angles (θ, ϕ) of the magnetic field, the Pake-doublet splittings (J_1, J_2, J_3, J_4), and the inner-outer splittings ($\delta_1, \delta_2, \delta_3, \delta_4$) at room temperature to be ($\theta \sim 6.6°$, $\phi \sim 24°$), ($J_1 \sim 1.8$, $J_2 \sim 1.8$, $J_3 \sim 3.6$, $J_4 \sim 3.6$), and ($\delta_1 \sim 15$, $\delta_2 \sim 17$, $\delta_3 \sim 13$, $\delta_4 \sim 15$) for 500h-0kbar-κCl; ($\theta \sim 14.3°$, $\phi \sim 90°$), ($J_1 \sim 1.2$, $J_2 \sim 1.2$, $J_3 \sim 1.2$, $J_4 \sim 1.2$), and ($\delta_1 \sim 12$, $\delta_2 \sim 20$, $\delta_3 \sim 12$, $\delta_4 \sim 20$) for 500h-5kbar-κCl; and ($\theta \sim 8.5°$, $\phi \sim 6°$), ($J_1 \sim 0.75$, $J_2 \sim 0.75$, $J_3 \sim 2.0$, $J_4 \sim 2.0$), and ($\delta_1 \sim 14$, $\delta_2 \sim 14$, $\delta_3 \sim 17$, $\delta_4 \sim 17$) for 0h-0kbar-κCl. The values of δ_i and J_i are in kHz.

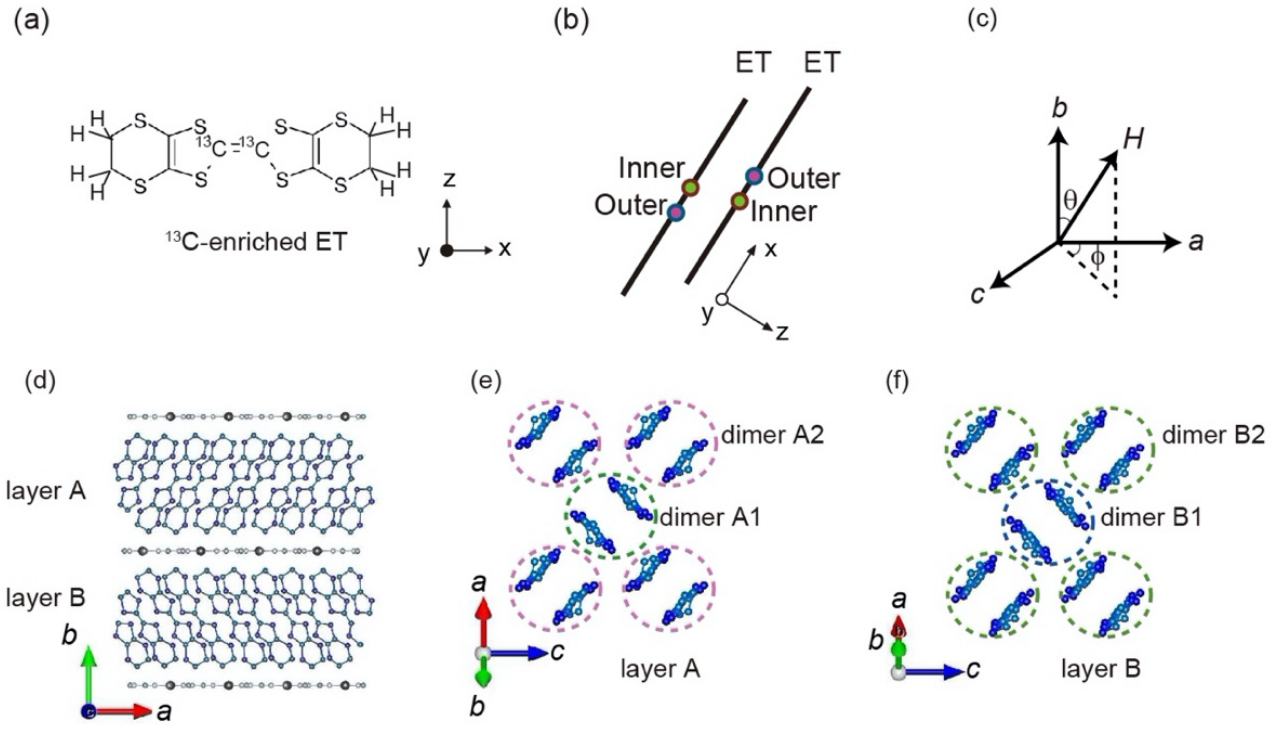

Fig. 3.3. (a) An ET molecule labeled with ^{13}C isotopes at the two central carbons. (b) ^{13}C nuclei at the inner and outer sites with different hyperfine fields in a dimer of ET molecules. (c) Crystallographic axes and my definition of the angles (θ, ϕ). Layered structure (d) and in-plane arrangements of the ET molecules in layers A and B in κCl (e, f). (This figure is published in Yamamoto *et al*., Phys. Rev. Lett. **124**, 046404 (2020).)

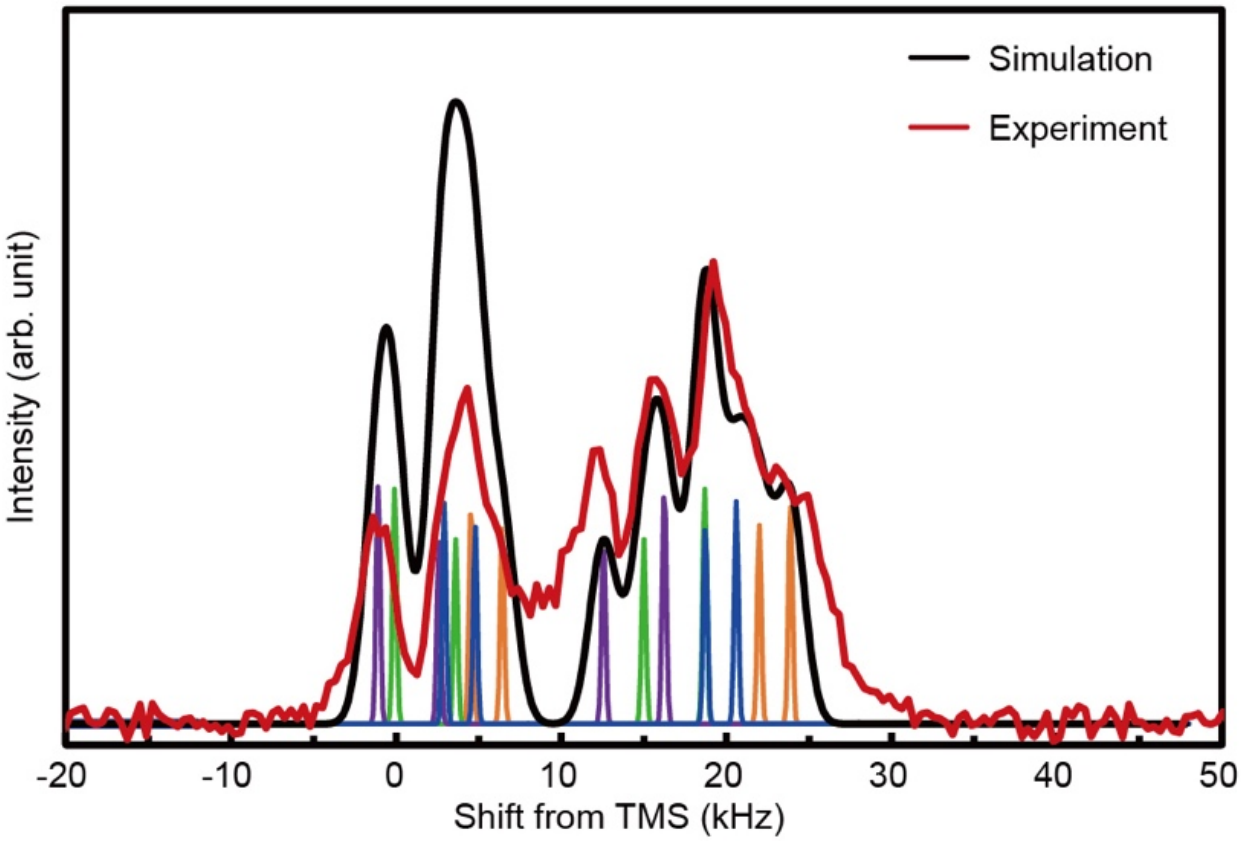

Fig. 3.4. ^{13}C-NMR spectrum for 500h-0kbar-κCl at 261 K. The red and black curves represent the experimentally obtained and simulated spectra, respectively. The latter is a superposition of the sixteen split lines, with line widths of 1.4 kHz, the origins of which are explained in the subsubsect. 3.2.4.1. The relatively large deviation of the simulated spectrum from the experimental spectrum at lower frequencies occurs for the following reason: The intensity of each spectral line is proportional to $\exp(-t/T_1')$, where T_1' is the spin-lattice relaxation time for each line, and t is the time interval between the saturation comb pulses and the $\pi/2$ pulse. In the present case, T_1' for the lower frequencies is longer than that for the higher frequencies. By chance I used a time t that was longer than the value of T_1' for the higher frequencies but shorter than that for the lower frequencies. The deviation, therefore, appears only at lower frequencies. (This figure is published in Yamamoto *et al*., Phys. Rev. Lett. **124**, 046404 (2020).)

3.2.4.2 Spin-spin relaxation rates

The spin-spin relaxation rates (the spin-echo decay rates) T_2^{-1} can be obtained from the decay of the spin-echo intensity $I(2\tau)$, where τ is the time interval between the π/2 and π pulses. However, as shown in Figs. 3.5(a-j), the $I(2\tau)$ curves in the present study exhibit complicated damped oscillations, which make it difficult to obtain the decay properties. Because κCl has four different inequivalent ET dimers in a magnetic field, $I(2\tau)$ is given by

$$I(2\tau) = D(2\tau)\sum_{i=1}^{4} O_i(2\tau), \tag{3-3}$$

where $O_i(2\tau)$ is the oscillating term of the spin-echo signal for i th ET dimer in the unit cell, and $D(2\tau)$ is the decay term. Thus, to obtain T_2 from the decay term, it is necessary to determine $O_i(2\tau)$. It is known that $O_i(2\tau)$ oscillates according to the following relation [107],

$$O_i(2\tau) \propto \cos(\omega_{i\alpha}\cdot 2\tau) - \frac{J_i}{4\Delta_i}\left(1-\frac{J_i}{2\Delta_i}\right)\cos(\omega_{i\beta}\cdot 2\tau) + \frac{J_i}{4\Delta_i}\left(1+\frac{J_i}{2\Delta_i}\right)\cos(\omega_{i\gamma}\cdot 2\tau), \tag{3-4}$$

where $\omega_{i\alpha} = 2\pi\cdot\frac{J_i}{2}$, $\omega_{i\beta} = 2\pi\cdot\frac{J_i-\Delta_i}{2}$, $\omega_{i\gamma} = 2\pi\cdot\frac{J_i+\Delta_i}{2}$, and $\Delta_i = \frac{\sqrt{J_i^2+4\delta_i^2}}{2}$.

For $\delta_i >> J_i$, only the first term is relevant, and the oscillations can then be approximated by

$$O_i(2\tau) \propto \cos(\omega_{i\alpha}\cdot 2\tau) = \cos\left(2\pi\cdot\frac{J_i}{2}\cdot 2\tau\right). \tag{3-5}$$

For the present experiment (H = 8.0 T), I do indeed have $\delta_i >> J_i$, as discussed in the previous subsubsect. 3.2.4.1. Using the values of J_i determined in the subsubsect. 3.2.4.1, I calculated $O_i(2\tau)$ and confirmed that the calculation reproduces well the oscillation of the $I(2\tau)$ curve, as shown in Fig. 3.5(a). Because I succeeded in confirming the validity of the above single-frequency-oscillation analysis, I fitted the total spin-echo intensity curve $I(2\tau)$ to the following relation to obtain T_2:

$$I(2\tau) = C\left\{\sum_{i=1}^{4}\cos\left(2\pi\cdot\frac{J_i}{2}\cdot 2\tau\right) + B\right\}\cdot\exp\left\{-\left(\frac{2\tau}{T_2}\right)^2\right\}, \tag{3-6}$$

where C and B are fitting parameters, and the J_i are fixed at the values determined in the subsubsect. 3.2.4.1. Here the small temperature-independent term B corresponds to the non-oscillating background of the observed spin-echo signal, which may be due to imperfect refocusing of the spin-echo. The spin-spin relaxation (spin-echo decay) is caused by two mechanisms: (a) magnetic interactions between like nuclei (nuclei with almost the same Larmor frequencies) and (b) fluctuations of the internal magnetic field in the kHz frequency range. Strictly speaking, these mechanisms cause slightly different relaxation of the magnetization of the nuclei: (a) Gaussian decay,

$$I(2\tau) \propto \exp\left\{-\left(\frac{2\tau}{T_{2g}}\right)^2\right\}, \tag{3-7}$$

and (b) exponential decay,

$$I(2\tau) \propto \exp\left(-\frac{2\tau}{T_{2l}}\right). \tag{3-8}$$

In principle, I should therefore take the decay term $D(2\tau)$ to be the product of the Gaussian and exponential functions, with T_{2g} and T_{2l} :

$$D(2\tau) \propto \exp\left\{-\left(\frac{2\tau}{T_{2g}}\right)^2\right\} \cdot \exp\left(-\frac{2\tau}{T_{2l}}\right). \tag{3-9}$$

Nevertheless, I have assumed only the Gaussian function

$$D(2\tau) \propto \exp\left\{-\left(\frac{2\tau}{T_2}\right)^2\right\} \tag{3-10}$$

as the decay term, thus obtaining T_2^{-1}, which contains information about both T_{2g}^{-1} and T_{2l}^{-1}. I did this because the latter fit has only one fitting parameter, which can be determined more precisely, and which can capture the qualitative properties of T_{2l}^{-1} owing to the temperature-independence of T_{2g}^{-1} in the present system.

Note that I fitted the following relation to the spin-echo intensity $I(2\tau)$ of the inner-site ^{13}C nuclei for 0h-0kbar-κCl below T_N:

$$I(2\tau) = C \exp\left\{-\left(\frac{2\tau}{T_2}\right)^2\right\}. \tag{3-11}$$

Below T_N, the nuclear spins of the inner and outer ^{13}C nuclei did not resonate simultaneously under the present experimental conditions. This is because the frequency range to be covered by the π/2 and π pulses was approximately 100 kHz, which was smaller than the ~300 kHz difference between the Larmor frequencies of the inner and outer ^{13}C nuclei. (This large difference between the hyperfine fields of the inner and outer ^{13}C nuclei results from local spontaneous magnetization of the order of $0.5\mu_B$ and different hyperfine couplings for the inner and outer ^{13}C nuclei.) In other words, the inner and outer ^{13}C nuclei can be regarded as unlike-nuclei below T_N in the present experiment, and thus the spin-echo intensities do not oscillate (Figs. 3.5(k, l)).

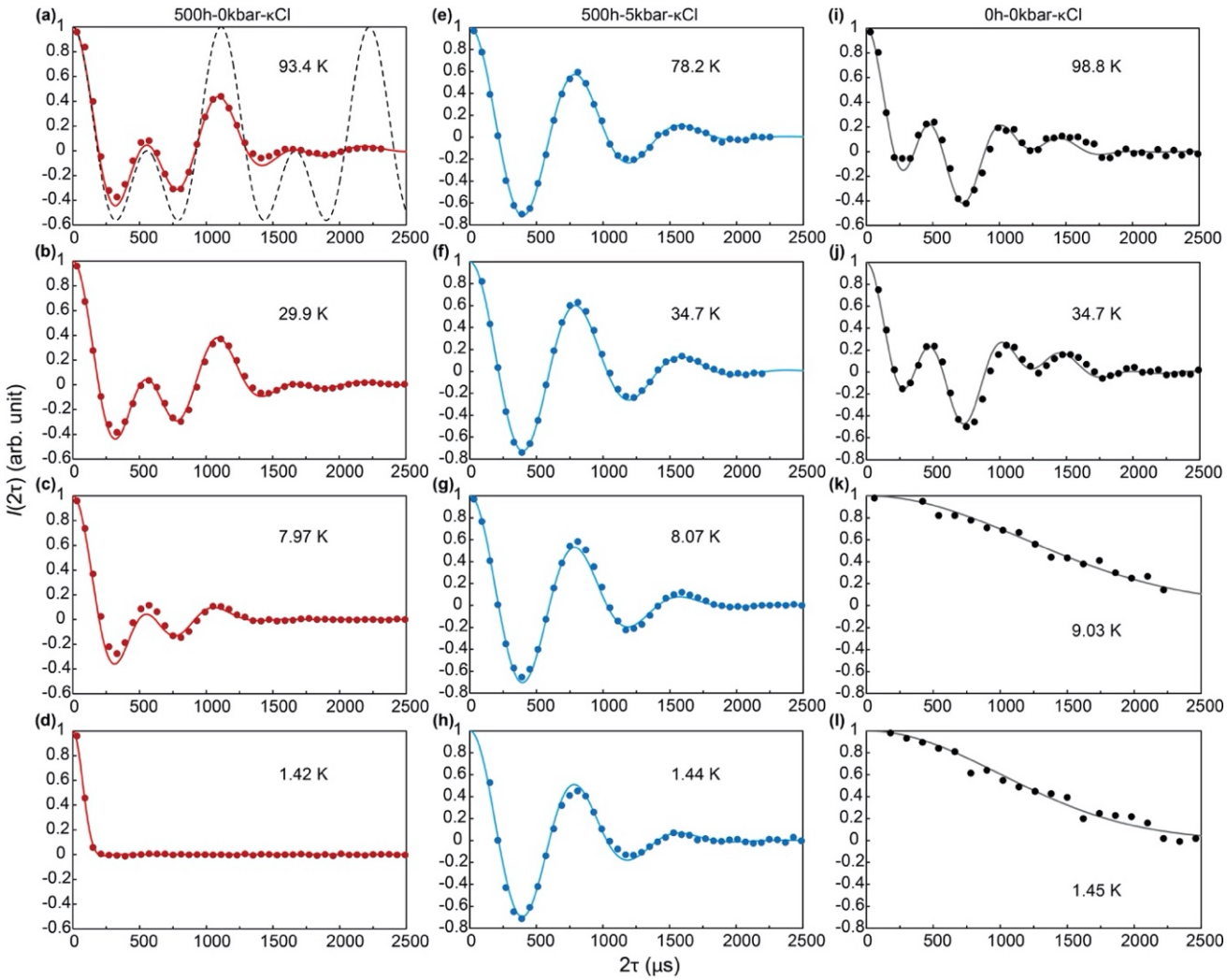

Fig. 3.5. Spin-echo signal $I(2\tau)$ for 500h-0kbar-κCl (a-d), 500h-5kbar-κCl (e-h), and 0h-0kbar-κCl (i-l). The bold lines show the curves fitted to $I(2\tau)$. The broken line in (a) indicates the oscillating part of the fitted curve. (This figure is published in Yamamoto *et al*., Phys. Rev. Lett. **124**, 046404 (2020).)

3.2.4.3 T_{2g}^{-1} caused by magnetic interactions between like-nuclei

As mentioned above, magnetic interactions between like-nuclei cause spin-echo decay at the rate T_{2g}^{-1}. I discuss and evaluate this decay rate in this subsubsection. Note that the nuclear-dipole couplings between adjacent ^{13}C nuclei result in the oscillation of the spin-echo intensity, as explained in the subsubsect. 3.2.4.2. To be precise, the rate T_{2g}^{-1} in the present system originates from the nuclear-dipole coupling between ^{13}C nuclei belonging to different ET molecules. Accordingly, by using the crystal structure of the present system I roughly estimated the value of T_{2g}^{-1} resulting from these couplings, obtaining

$$T_{2g}^{-1} \sim \sum_i \frac{\mu_0 \gamma^2 \hbar}{R_i^3} \sim 1000 \text{ sec}^{-1}, \tag{3-12}$$

where μ_0 is the vacuum permeability, and the R_i are the distances between ^{13}C nuclei. The estimated value is close to the observed temperature-independent value of T_2^{-1}, as shown below.

I also note that in the present system the indirect nuclear spin-spin interaction mediated by the electrons does not contribute to T_{2g}^{-1}. This contribution is on the order of

$$A^2 \chi(q)_{\max} \left(\frac{h}{g N_A \mu_B^2} \right), \tag{3-13}$$

where A is the hyperfine coupling constant, $\chi(q)_{\max}$ is the maximum value of the q-dependent susceptibility of the electrons, h is the Planck constant, g is the g-factor of the electrons, N_A is the Avogadro number, and μ_B is the Bohr magneton. For the parameters of the present system [$A \sim 7$ MHz/μ_B and $\chi(0) \sim 2.5\times10^{-4}$ emu/mol [18]], I estimated the value of T_{2g}^{-1} due to the indirect nuclear spin-spin interaction to be approximately 0.6 s^{-1}, which is 10^3–10^4 times smaller than the observed value of T_{2g}^{-1}. Thus, the indirect contribution is negligible unless $\chi(q)/\chi(0)$ at a certain wavenumber q exceeds 10^3–10^4, which is unrealistic, and T_2^{-1} in this work only measures the electron fluctuations on a kHz scale and the nuclear-nuclear magnetic-dipole coupling.

3.3 Results and Discussion

3.3.1 Spectra

Figure 3.6 shows the ^{13}C-NMR spectra of 0h-0kbar-κCl, 500h-0kbar-κCl, and 500h-5kbar-κCl crystals. The ^{13}C-NMR spectra reflect the static internal magnetic fields on the ^{13}C nuclei. The spectra of 0h-0kbar-κCl (Fig. 3.6(a)) show significant shifts and broadening below the antiferromagnetic transition temperature T_N (~30 K under ~8.0 T [108]) because of the ordered moments. Note that the actual spectra consist of four peaks but unfortunately, I could not obtain the other two, which are on the higher frequency side. In contrast, for the 500h-0kbar-κCl sample (Fig. 3.6(b)), the spectra show no shift over the entire measured temperature range. Although the spectra exhibit broadening at low temperatures, the internal magnetic field is much smaller than that in the antiferromagnetic phase in 0h-0kbar-κCl. These features confirm that the 500-h x-ray irradiation extinguishes the antiferromagnetic long-range order, as proposed from the ^{1}H-NMR study [103]. When I applied 5 kbar to the x-ray-irradiated sample (Fig. 3.6(c)), the spectra showed no appreciable change over the entire measured temperature range. This is because the system is located deep in the metallic phase without superconductivity [104].

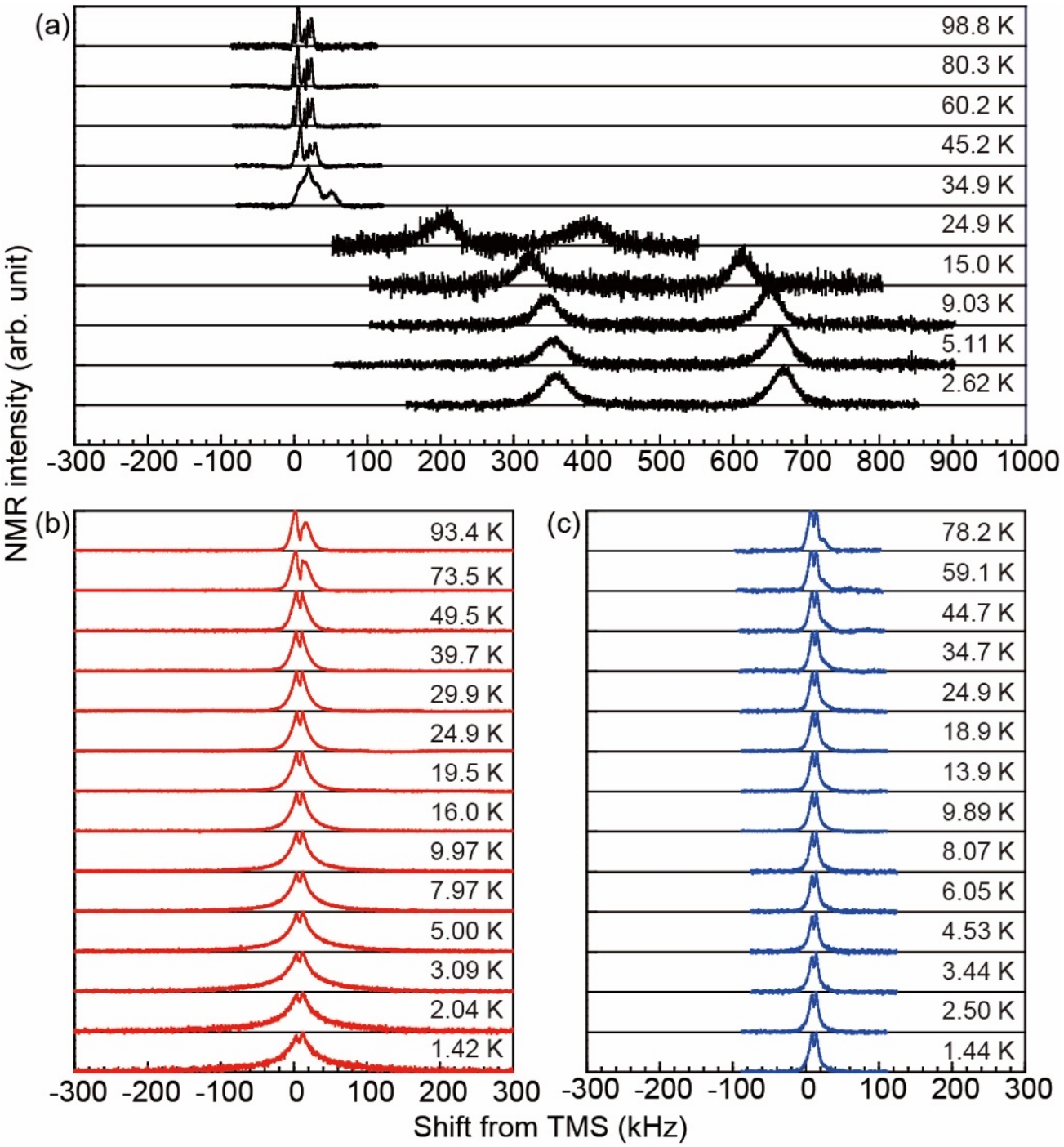

Fig. 3.6. ^{13}C-NMR spectra. The spectra of 0h-0kbar-κCl (a) 500h-0kbar-κCl, (b) and 500h-5kbar-κCl, (c) crystals. The shifts are relative to tetramethylsilane (TMS). (This figure is published in Yamamoto *et al*., Phys. Rev. Lett. **124**, 046404 (2020).)

3.3.2 Spin-lattice relaxation rate T_1^{-1}

Figure 3.7 shows the temperature dependence of T_1^{-1} of the 0h-0kbar-κCl, 500h-0kbar-κCl, and 500h-5kbar-κCl samples. The relaxation rate T_1^{-1} reflects the magnitude of the fluctuations of the internal magnetic fields on the ^{13}C nuclei on a MHz scale. For the 0h-0kbar-κCl sample, T_1^{-1} shows a peak around T_N; this peak indicates the critical slowing down that accompanies the magnetic transition [18,109]. In contrast, for the 500h-0kbar-κCl sample, T_1^{-1} does not show any peak structure over the entire measured temperature range. This feature also indicates that the x-ray irradiation causes the disappearance of the antiferromagnetic long-range order. Note that the slope of T_1^{-1} below 30 K ($T_1^{-1} \propto T^{0.4}$) almost reproduces the previous ^{1}H-NMR result ($T_1^{-1} \propto T^{0.5}$) [103]. The slight discrepancy between the exponents is most likely attributed to the different sensitivity to the electronic state, which was explained previously. When 5 kbar is applied to the x-ray-irradiated sample, T_1^{-1} for the 500h-5kbar-κCl sample is proportional to the temperature and follows the Korringa relation, at least up to 100 K. This behavior clearly indicates that the system has a nonzero density of states at the Fermi energy and lies deep in the metallic side, which is far from the Mott boundary. This result is consistent with the result of the spectra and the fact that 500-h x-ray irradiated κ-$(ET)_2Cu[N(CN)_2]Br$ shows a metallic resistivity under pressures more than ~1 kbar [104].

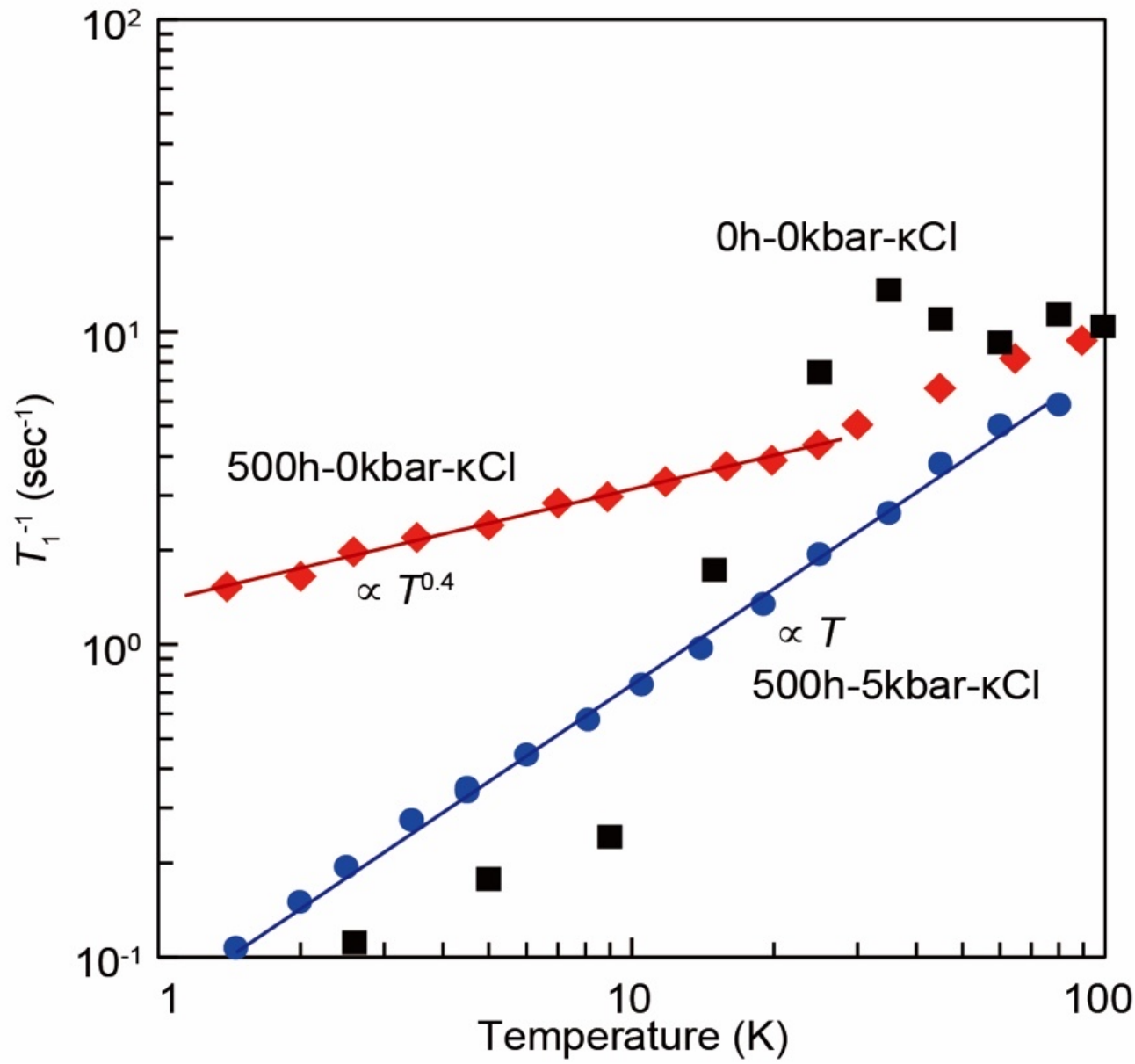

Fig. 3.7. Temperature dependence of the ^{13}C-NMR spin-lattice relaxation rate of 0h-0kbar-κCl, 500h-0kbar-κCl, and 500h-5kbar-κCl crystals. (This figure is published in Yamamoto *et al*., Phys. Rev. Lett. **124**, 046404 (2020).)

As mentioned above, I fitted the spin-lattice relaxation curves, $1-M(t)/M(\infty)$ vs. t, using the stretched-exponential function, $\exp\{-(t/T_1)^{\beta}\}$, where β is the stretching exponent. The exponent is unity for the single-exponential relaxation but would decrease with an increasing distribution of T_1.

Figure 3.8 shows the temperature dependence of β for 500h-0kbar-κCl and the relaxation curves. The observed exponent deviates from unity even at high temperatures. This occurs because the present system under the magnetic field has 16 inequivalent ^{13}C sites, and the observed nuclear magnetization is evaluated as the overall integration of signals from all the sites. Below 20 K, a further decrease in β implies a slight enhancement of inhomogeneity in the electronic state.

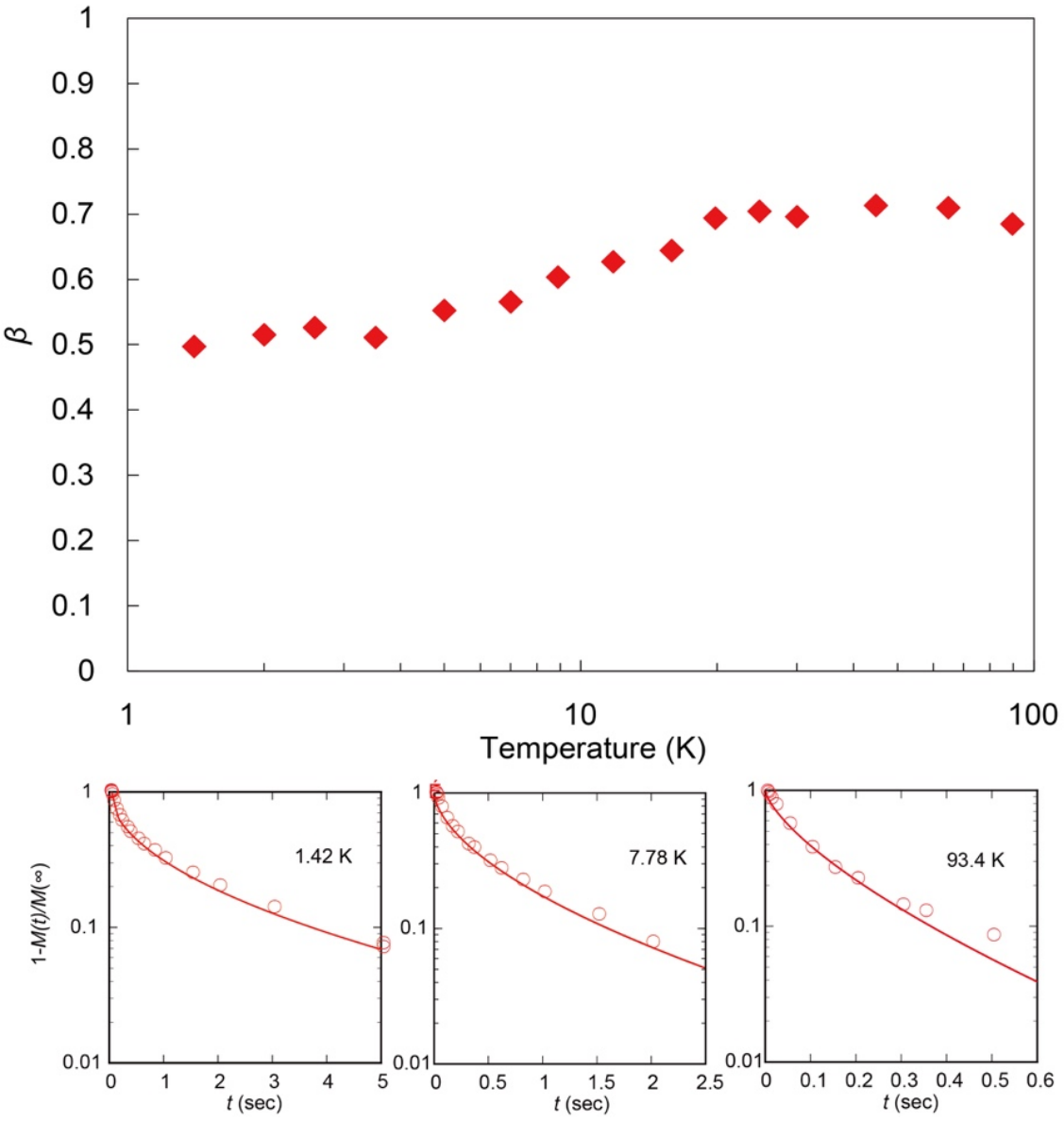

Fig. 3.8. Temperature dependence of stretching exponent β for 500h-0kbar-κCl. The spin-lattice relaxation curves at three representative temperatures are presented in the lower three panels. (This figure is published in Yamamoto *et al.*, Phys. Rev. Lett. **124**, 046404 (2020).)

3.3.3 Spin-spin relaxation rate T_2^{-1}

Figure 3.9 shows the temperature dependence of T_2^{-1} of the 0h-0kbarκCl, 500h-0kbar-κCl, and 500h-5kbar-κCl samples. The spin-spin relaxation rate in κCl is expressed as the sum of a temperature-dependent component T_{2l}^{-1} and a temperature-independent component T_{2g}^{-1} [$T_2^{-1}(T) = T_{2l}^{-1}(T) + T_{2g}^{-1}$], which measure, respectively, the electron fluctuations on a kHz scale and the nuclear-nuclear magnetic-dipole coupling, as described above. In addition, taking the crystal structure of κCl into account, I estimated T_{2g}^{-1} to be approximately 1000 s^{-1}.

In usual electronic states, where electron dynamics is frequency-independent below the THz scale, the amplitudes of the dynamics in the kHz and MHz regions are generally almost the same, hence $T_{2l}^{-1} \sim T_1^{-1}$. If this is the case in the present material, then T_2^{-1} is dominated by T_{2g}^{-1}, because T_{2l}^{-1} ($\sim T_1^{-1}$, as shown in Fig. 3.7) is much smaller than T_{2g}^{-1}. Indeed, for the 0h-0kbar-κCl sample, T_2^{-1} has the temperature-independent value of ~ 1000 s^{-1} over the entire measured temperature range, which clearly means that T_2^{-1} is dominated by T_{2g}^{-1}. In contrast, for the 500h-0kbar-κCl sample, T_2^{-1} increases dramatically below ~10 K. This is due to a drastic increase in T_{2l}^{-1} because T_{2g}^{-1} is caused by nuclear-nuclear magnetic-dipole coupling and thus is constant. In this sample, T_{2l}^{-1} (kHz dynamics) increases with cooling, whereas T_1^{-1} (MHz dynamics) decreases, as seen in Figs. 3.7 and 3.9. The ratio of T_{2l}^{-1} to T_1^{-1} (kHz dynamics to the MHz dynamics) exceeds 10^3 at the lowest measured temperature. These results demonstrate that introducing randomness produces an unusual electronic state with an extraordinary enhancement of dynamics in frequency regions much slower than the THz scale characterized by the energy scale of the original Hamiltonian. Importantly, this peculiar electronic state disappears when the system is displaced from the Mott boundary by applying pressure; as shown in Fig. 3.9, the 500h-5kbar-κCl sample shows no such enhancement in T_2^{-1}. This clearly suggests that the emergence of the slow dynamics is caused not by the randomness alone but by the combination of closeness to the Mott boundary and randomness.

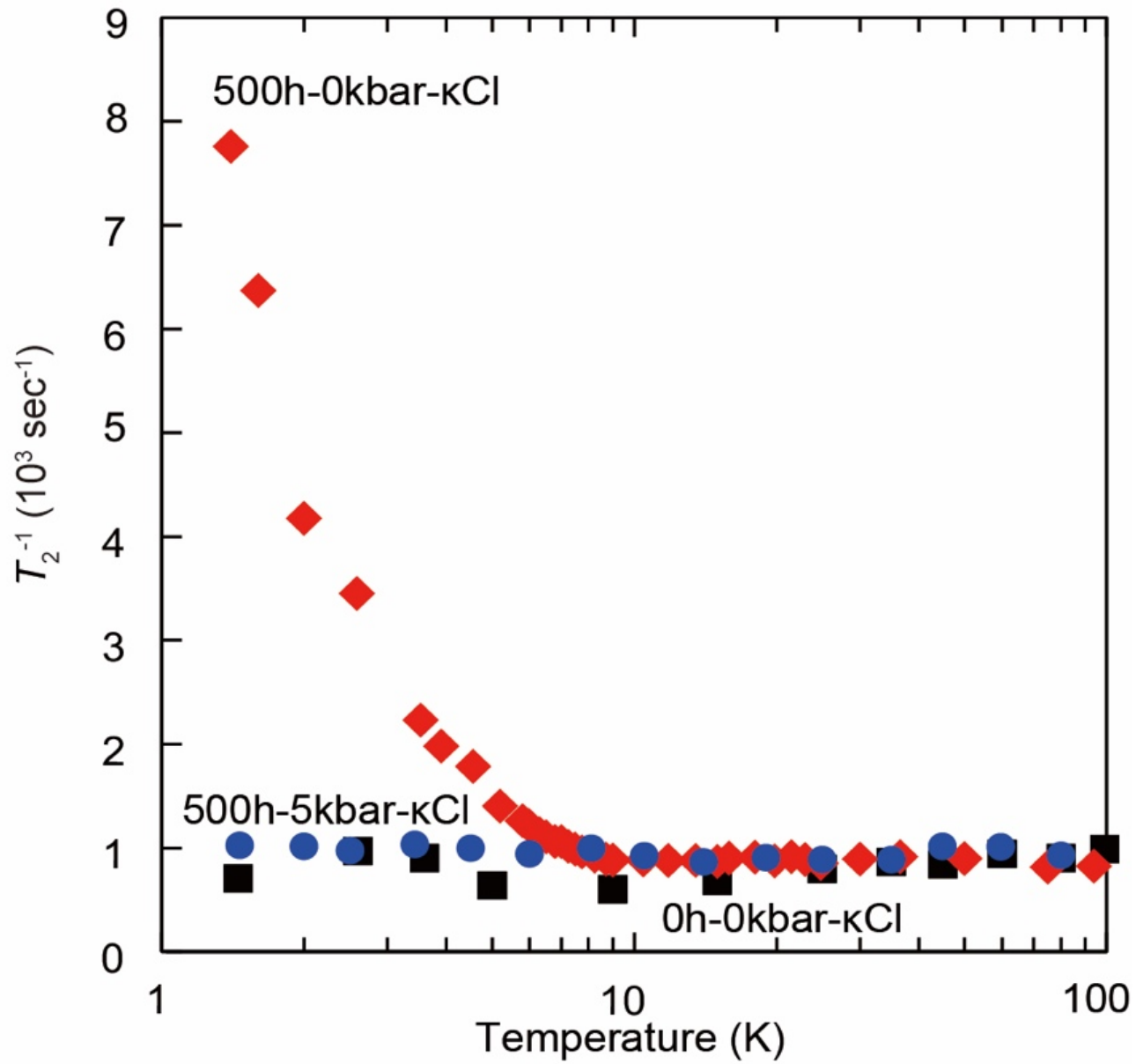

Fig. 3.9. Temperature dependence of the ^{13}C-NMR spin-spin relaxation rate of 0h-0kbar-κCl, 500h-0kbar-κCl, and 500h-5kbar-κCl crystals. (This figure is published in Yamamoto *et al.*, Phys. Rev. Lett. **124**, 046404 (2020).)

3.3.4 Contribution of ethylene-group dynamics

The terminal ethylene groups of an ET molecule fluctuate between the two conformations at high temperatures as shown in Fig. 3.10(a), and the vibrations are frozen around 70 K for κCl [110−112]. Accordingly, fast cooling through 70 K (typically faster than 1 K/min) causes the quenched disorder of random conformations of the ethylene groups, which affects the low-temperature electronic state [113, 114]. To avoid the disorder effect from the ethylene groups, I set the cooling-rate less than 0.1 K/min around 70 K.

Here I discuss the effect of the x-ray irradiation on the properties of the thermally activated dynamics of the ethylene groups. I performed ^{1}H-NMR measurements for the present (^{13}C-enriched) 500h-0kbar-κCl sample. Figure 3.10(b) shows the temperature dependence of ^{1}H-NMR T_1^{-1} and $T_1^{-1}{}_{mol} = T_1^{-1} - T_1^{-1}{}_{el}$, where $T_1^{-1}{}_{mol}$ and $T_1^{-1}{}_{el}$ are the contribution from the dynamics of the ethylene groups and electrons, respectively. For comparison, I also show the data previously reported for a (^{13}C-*non*enriched) 500-h irradiated κCl sample [103] and the data for non-irradiated κCl [18]. The data for the two 500-h irradiated κCl samples are fairly well reproduced.

It was reported that, for non-irradiated κCl, a steep increase in T_1^{-1} above 200 K is attributed not to electronic origin but the conformational dynamics of the ethylene groups with an activation energy Δ of 2600±100 K [18]. The enhancements of T_1^{-1} for the non-irradiated and 500h-irradiated samples are quantitatively similar. To evaluate how the x-ray irradiation affects the dynamics of the ethylene groups, I derived the activation energy of the dynamics of the ethylene groups for the 500h-irradiated samples by using the Bloembergen-Purcell-Pound analysis, as well as the previous study [18]. I obtained Δ of 2600±100 K for these two 500-h irradiated samples, which is indicative of the insensitivity of the dynamics of the ethylene groups to the x-ray irradiation.

Furthermore, ^{13}C-T_2^{-1} for the present 500h-0kbar-κCl sample shows a peak anomaly around 135 K due to the slowing down of the dynamics of the ethylene groups (see Fig. 3.10(c)). This peak temperature is almost the same as that for non-irradiated κCl [115].

These ^{1}H-T_1^{-1} and ^{13}C-T_2^{-1} results mean that the x-ray irradiation does not alter the dynamics of the ethylene groups. Thus, for 500h-0kbar-κCl, the dynamics of the ethylene groups is quenched below 70 K and the Hamiltonian of the electronic system at low temperatures is not dynamic but static. Therefore, the low-temperature slow dynamics observed in T_2^{-1} as described above originates not from the molecular motion.

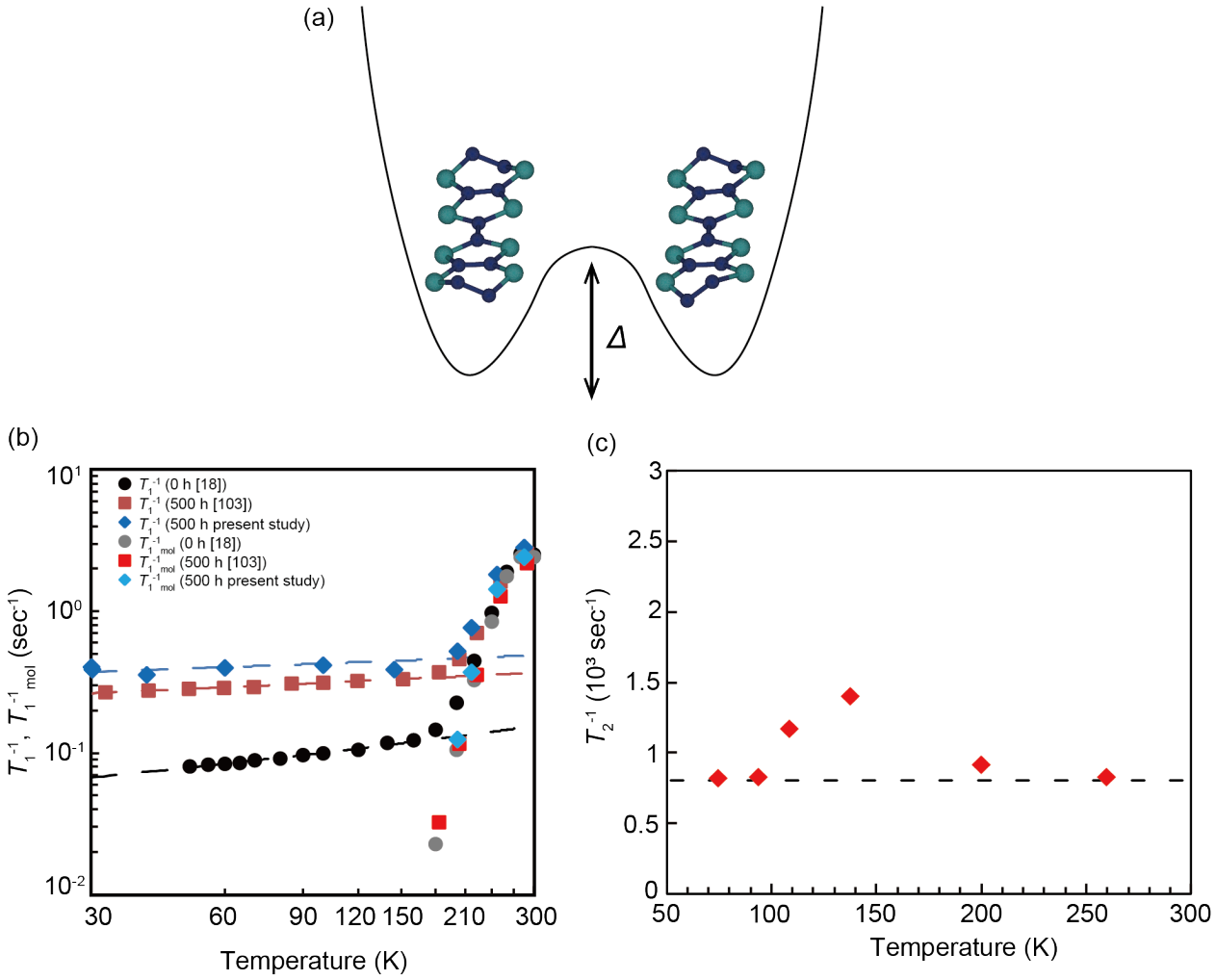

Fig. 3.10. The conformations of the terminal ethylene groups of an ET molecule and the contribution of the ethylene dynamics to NMR relaxations. (a) The conformations of the ethylene groups and schematic potential diagram with an activation energy Δ. (b) Temperature dependence of ^{1}H-NMR T_1^{-1} and $T_1^{-1}{}_{\rm mol} = T_1^{-1} - T_1^{-1}{}_{\rm el}$. The diamonds correspond to the data for 500h-0kbar-κCl under 3.1 T. The circles (squares) are from the previous study of a nonirradiated (500-h irradiated) κCl crystal under 3.7 T [18, 103]. The dashed lines are power-law fits to T_1^{-1} between 30 K and 150 K and their extrapolations to high temperatures, which indicate the electronic contributions $T_1^{-1}{}_{\rm el}$. (c) Temperature dependence of ^{13}C-NMR T_2^{-1} for 500h-0kbar-κCl above 50 K. The dashed line shows T_{2g}^{-1}, which is the contribution from the nuclear-dipole coupling. (This figure is published in Yamamoto *et al.*, Phys. Rev. Lett. **124**, 046404 (2020).)

3.3.5 Contribution of domain wall dynamics

In general, a system in the vicinity of a boundary between two phases separated by a first-order phase transition sometimes shows macroscopic phase separation and thus has domain walls between the two phases. In this case, domain-wall dynamics causes slow dynamics only at sites near the domain walls. In my experiment, the slow dynamics is detected in T_2^{-1}, which indicates that all sites exhibit slow dynamics, in contrast to the case of domain-wall dynamics.

Furthermore, the spectra of the 500h-0kbar-κCl sample (Fig. 3.6(b)) obviously differ from those of slightly pressurized 0h-κCl and deuterated κ-$(ET)_2Cu[N(CN)_2]Br$ (d^8-Br), which are on the Mott boundary and which show phase separation between the metallic phase and the Mott-insulating (antiferromagnetic long-range-ordered) phase [116,117]; for slightly pressurized 0h-κCl and d^8-Br at low temperatures, the spectrum consists of two clearly distinguishable spectral components, which originate from the metallic domain and the antiferromagnetic long-range-ordered insulating domain. The latter component has a huge shift, similar to the spectra of 0h-0kbar-κCl shown in Fig. 3.6(a). This result also means that the entire 500h-0kbar-κCl sample does not undergo macroscopic phase separation.

Therefore, these results mean that the present slow dynamics is not attributable to conventional domain-wall motion but attributable to electrons.

3.3.6 Proposal for the concept of the electronic Griffiths phase

As discussed so far, the present system shows extraordinarily slow electron dynamics, even though it does not have any long-range order or macroscopic phase separation. This result looks contrary to the common sense of solid-state physics because in the conventional understanding in solid-state physics the absence implies that the system does not have any new length-scale, and consequently, any new energy-scale. In this context, the present phase with slow dynamics is an unusual state, which cannot be explained by the conventional understanding. The key to understand the present peculiar phase with slow dynamics is that it is realized only when the system meets two factors simultaneously: (i) *an electronic system is located near the Mott boundary* and (ii) *the electronic system contains randomness.* These two factors lead to the idea that the present peculiar phase can be explained by the electronic version of the concept of the "*Griffiths phase*," which was proposed originally in magnetism physics [118]. Thus, I named the peculiar electronic phase an "*electronic* Griffith phase."

When randomness is introduced into a system that exhibits a first-order transition with a critical endpoint, the temperature of the critical endpoint is decreased, eventually declining to zero. In this case, the region where the first-order transition originally existed is changed into a widely spread critical region, or the "Griffiths phase" [118,119]. This scenario was originally proposed for Ising spin systems [118]. Note that Mott-transition systems have a phase diagram similar to those of Ising spin systems. It is believed that the universality of the Mott-transition belongs to the Ising universality and it in κCl is related to the Ising universality; in a clean system, the phase boundary between the metallic state and the Mott-insulating state is a first-order transition with a finite-temperature critical endpoint, as described in the subsect. 1.1.3. My result provides experimental evidence that the Griffiths scenario is also applicable to Mott-transition systems, as has been proposed by theoretical works that examined the disordered Hubbard model [120−123]. The concept of the electronic Griffiths phase explains the above two conditions naturally. Recently, it has been reported that x-ray irradiation of the present material decreases both the temperature and pressure of the endpoint [124,125]. Because the Griffiths phase generally appears in the region where an original state in a clean system is changed into another state by randomness [119], I speculate that the electronic Griffiths phase should spread roughly over the region swept by the first-order transition line when randomness is introduced, as shown in Fig. 3.11.

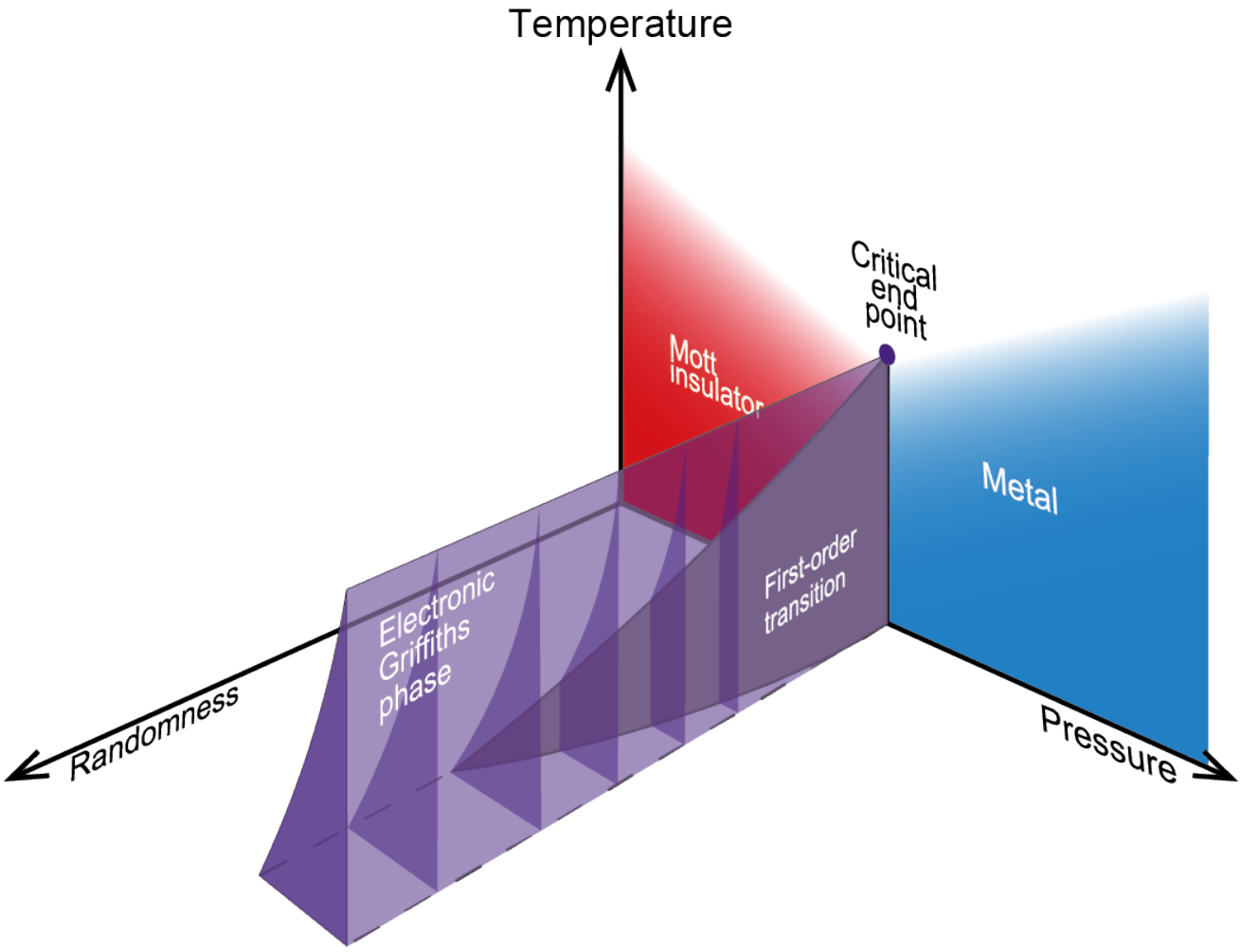

Fig. 3.11. Schematic phase diagram of the Mott transition in temperature-pressure-randomness space.

3.3.7 Expansion of the concept of the electronic Griffiths phase

The term “electronic Griffiths phase,” which means a Griffiths phase not in magnetic systems but electronic systems, has already been proposed in disordered Kondo systems [123]. When randomness is introduced to Kondo systems, Kondo temperature (T_K) becomes distributed [126]. It has also been discussed that, in the case of strong randomness, the distribution of T_K spreads down to zero and causes non-Fermi-liquid behavior. This is the Kondo-based electronic Griffiths scenario. This scenario was sparked by the early experimental work by O. O. Bernal *et al*. [127] and developed by several theoretical works [123,128−136], although real candidate materials are very limited even now [137−140]. In this context, my work on the Mott transition system provides another class of the electronic Griffiths phase, which is seemingly different from the Kondo-based electronic Griffiths phase.

These two Griffiths phases should have the same underlying physics. The distribution of T_K has been regarded as a key factor to realize the Kondo-based electronic Griffiths physics. However, it has been pointed out that more fundamental is the distribution of a quasiparticle weight to zero [120,123,131]. This distribution of a quasiparticle weight to zero corresponds to the distribution of effective mass up to infinity, which is responsible for the non-Fermi-liquid behavior and the divergence of low-frequency electron dynamics. Therefore, because the disappearance of the quasiparticle weight is one of the key factors of Mott transition as explained in the subsect. 1.1.1, the same physics can be realized not only in disordered Kondo systems but also in disordered Mott systems; the electronic Griffiths phase realized in Mott transition systems may be closely related to the electronic Griffiths phase in Kondo systems.

As discussed above, the Griffiths scenario can be a broader concept than has been considered before. Besides, the Griffiths scenario may be a key concept for understanding inhomogeneous electronic states realized in cuprates [77-86] and manganites [87-94]. Upon changing a parameter such as a carrier concentration, they sometimes show spatially inhomogeneous electronic states with static structures (nanoscale-structures, mesoscopic domains, and/or spatially inhomogeneous structures) and spin and/or charge slow dynamics accompanied by these structures, which are similar to my finding. These inhomogeneous states are realized by the competition between different ground states and the original boundaries between these states in these inorganics would also be first-order transitions in the absence of randomness. Therefore, the inhomogeneous states realized in the inorganics possibly have similar underlying physics.

In the present study, I captured only slow dynamics in the organic system. It is interesting and a future problem whether the present organic system also has a spatially inhomogeneous structure, for

example in the quasiparticle weight.

Lastly, I note that there is a difference between the present organic system and these inorganics in the nature of the first-order transition. In the present organic system, the first-order transition has a critical endpoint, as explained in the subsect. 1.1.3. In contrast, in these inorganics, first-order transitions between different competing phases should not have critical endpoints, because the competing phases have different symmetry. Therefore, though I think that the spatially inhomogeneous electronic states in the inorganics may have similar physics to the electronic Griffiths phase observed in the present organic system, it is natural to think that the details may be different. I hope that this work stimulates further experimental and theoretical research on this issue.

3.4 Conclusion

Through detailed ^{13}C-NMR studies, I demonstrate that the antiferromagnetic long-range ordered state in κCl is completely suppressed in 500h-x-ray-irradiated κCl, and instead an anomalous paramagnetic insulating state (a putative disorder-induced spin liquid) shows up. Spin-lattice relaxation-rate (T_1^{-1}) measurements, which pick up the dynamics in the MHz region, found no anomaly in this paramagnetic state. By contrast, spin-spin-relaxation rate (T_2^{-1}) measurements, which see the dynamics in the kHz region, revealed that there is an anomalously slow electronic fluctuation that grows upon cooling in x-ray-irradiated κCl but not in nonirradiated κCl. Furthermore, the fluctuation can be easily suppressed upon applying a small pressure and pushing the system away from the critical region towards a metallic phase. These two findings clearly indicate that the observed slow electronic dynamics is induced by the disorder and develops exclusively near the Mott boundary. I proposed that this peculiar electronic state can be explained by the concept of the "electronic Griffiths phase", which is the expansion of the Griffiths phase proposed in magnetism physics into electronic systems.

4 Concluding Remarks

By using the superior controllability in organic systems, I have succeeded in clarifying two phenomena which are directly related to, or realized in the vicinity of, the Mott transition.

Using the controllability of electron correlation in $EtMe_3P[Pd(dmit)_2]_2$, I clarified the dimensionality of the superconductivity realized in this material, which has a layered structure with a nearly isotropic triangular lattice.

Correlated superconductivity on an isotropic triangular lattice is expected to exhibit exotic superconductivity. Besides, $EtMe_3P[Pd(dmit)_2]_2$ at ambient pressure shows the valence bond solid state (quantum nonmagnetic state) at low temperature, and the superconductivity in $EtMe_3P[Pd(dmit)_2]_2$ under pressure is adjacent to it, in contrast to the majority of other correlated superconductivities. Thus, the superconducting properties of $EtMe_3P[Pd(dmit)_2]_2$ are fascinating and need to be clarified, although little has been reported on them.

Here, I revealed the dimensionality of superconductivity in $EtMe_3P[Pd(dmit)_2]_2$. I concluded that layered superconductor $EtMe_3P[Pd(dmit)_2]_2$ is an anisotropic three-dimensional superconductor even at temperatures much lower than T_c (even at ~0.5 T_c), in contrast to the majority of other layered correlated-electron superconductors such as high-T_c cuprates and κ-$(ET)_2X$ systems, which show a dimensional crossover near T_c.

This present study opens an avenue for the full understanding of the superconductivity in $EtMe_3P[Pd(dmit)_2]_2$. I hope that this study will stimulate further research, such as a discussion on the symmetry of the Cooper pair.

Using the controllability of electron correlation and randomness of the Mott transition system κ-$(ET)_2Cu[N(CN)_2]Cl$, I studied the synergistic effect of the correlation and randomness.

Correlated electrons are sometimes found to show a spatially inhomogeneous phase, which is accompanied by extraordinarily slow electron dynamics. Such a phenomenon is rather similar to those observed in soft-matter systems. It is believed that the soft-matter-like behavior is very likely to be responsible for the colossal responses (such as colossal magnetoresistance) and to be related to the high-T_c physics. Despite its importance, however, very few systematic experimental studies have been undertaken to investigate the mechanism why correlated electrons show the soft-matter behavior in solid-matter.

Here, I revealed experimentally the condition under which correlated electrons show the soft-matter-

like behavior. I focused on an organic Mott-transition system κ-$(ET)_2Cu[N(CN)_2]Cl$ and have demonstrated that the soft-matter-like behavior is realized only when the following two factors are met simultaneously: i) an electronic system is near the metal/Mott-insulator boundary and ii) the system is subject to quenched disorder. This finding strongly suggests that the soft-matter-like behavior is explained by the concept of the "*electronic Griffiths phase*", which recently has been tried to be proposed theoretically.

This present experimental work will, I believe, shed light on the mechanism of the soft-matter behavior in solid matter and will stimulate a mutual exchange of the underlying physical concepts between the different two fields, namely, solid-state physics and soft-matter physics. Although what I demonstrated in this work is that this scenario is realized in a certain organic system, I believe that this concept can be applied to a large variety of correlated-electron materials such as cuprates and manganites.

Acknowledgment

I would like to express my sincere gratitude to my supervisor Prof. Tetsuaki Itou for his numerous help, and continuing support. I would also like to thank Dr. Tetsuya Furukawa (Tohoku University, IMR) for his help. The time I spent with them has helped me to grow the most in my life.

I would like to thank my collaborators Prof. Kazushi Kanoda, Dr. Kazuya Miyagawa (The University of Tokyo), Prof. Takahiko Sasaki (Tohoku University, IMR), and Prof. Reizo Kato (RIKEN) for their numerous supports.

I would like to thank all members of the Itou group, including past members. They have helped me to enjoy the last six years.

Finally, I would like to thank my family for their support.

Bibliography

[1] J. G. Bednorz and K. A. Müller, Z. Phys. B: Condens. Matter **64**, 189 (1986).

[2] N. F. Mott, Metal Insulator Transitions (Taylor& Francis, London, 1974)

[3] W. F. Brinkman and T. M. Rice, Phys. Rev. B **2**, 1324 (1970).

[4] X. Y. Zhang, M. J. Rozenberg, and G. Kotliar, Phys. Rev. Lett. **70**, 1666 (1993).

[5] C. Castellani, C. Di Castro, D. Feinberg, and J. Ranninger, Phys. Rev. Lett. **43**, 1957 (1979).

[6] G. Kotliar, E. Lange, and M. J. Rozenberg, Phys. Rev. Lett. **84**, 5180 (2000).

[7] G. Kotliar, S. Murthy, and M. J. Rozenberg, Phys. Rev. Lett. **89**, 046401 (2002).

[8] P. Limelette, A. Georges, D. Jérome, P. Wzietek, P. Metcalf, and J. M. Honig, Science **302**, 89 (2003).

[9] M. Imada, J. Phys. Soc. Jpn. **73**, 1851 (2004).

[10] F. Kagawa, K. Miyagawa, and K. Kanoda, Nature (London) **436**, 534 (2005).

[11] S. Papanikolaou, R. M. Fernandes, E. Fradkin, P. W. Phillips, J. Schmalian, and R. Sknepnek, Phys. Rev. Lett. **100**, 026408 (2008).

[12] L. Bartosch, M. de Souza, and M. Lang, Phys. Rev. Lett. **104**, 245701 (2010).

[13] M. de Souza, A. Brühl, Ch. Strack, B. Wolf, D. Schweitzer, and M. Lang, Phys. Rev. Lett. **99**, 037003 (2007).

[14] M. Abdel-Jawad, R. Kato, I. Watanabe, N. Tajima, and Y. Ishii, Phys. Rev. Lett. **114**, 106401 (2015).

[15] Y. Kawasugi, H. M. Yamamoto, N. Tajima, T. Fukunaga, K. Tsukagoshi, and R. Kato, Phys. Rev. B **84**, 125129 (2011).

[16] K. Kanoda and R. Kato, Annu. Rev. Condens. Matter Phys. **2**, 167 (2011).

[17] K. Kino and H. Fukuyama, J. Phys. Soc. Jpn. **65**, 2158 (1996).

[18] K. Miyagawa, A. Kawamoto, Y. Nakazawa, and K. Kanoda, Phys. Rev. Lett. **75**, 1174 (1995).

[19] Y. Shimizu, K. Miyagawa, K. Kanoda, M. Maesato, and G. Saito, Phys. Rev. Lett. **91**, 107001 (2003).

[20] Y. Shimizu, K. Miyagawa, K. Kanoda, M. Maesato, and G. Saito, Phys. Rev. B **73**, 140407(R) (2006).

[21] S. Lefebvre, P. Wzietek, S. Brown, C. Bourbonnais, D. Jérome, C. Mézière, M. Fourmigué, and P. Batail, Phys. Rev. Lett. **85**, 5420 (2000).

[22] F. Kagawa, T. Itou, K. Miyagawa, and K. Kanoda, Phys. Rev. B **69**, 064511 (2004).

[23] K. Kanoda, Physica C **282-287**, 299 (1997).

[24] A. Ardavan, S. Brown, S. Kagoshima, K. Kanoda, K. Kuroki, H. Mori, M. Ogata, S. Uji, and J. Wosnitza, J. Phys. Soc. Jpn. **81**, 011004 (2012).

[25] R. T. Clay and S. Mazumdar, Phys. Rep. **788**, 1 (2019).

[26] M. Lang, F. Steglich, N. Toyota, and T. Sasaki, Phys. Rev. B **49**, 15227 (1994).

[27] K. Kanoda, K. Miyagawa, A. Kawamoto, and Y. Nakazawa, Phys. Rev. B **54**, 76 (1996).

[28] R. H. McKenzie, Science **65**, 820 (1997).

[29] B. J. Powell and R. H. McKenzie, Phys. Rev. Lett. **94**, 047004 (2005) and references cited therein.

[30] M.-S. Nam, A. Ardavan, S. J. Blundell and J. A. Schlueter, Nature **449**, 584 (2007).

[31] Y. Shimizu, H. Akimoto, H. Tsujii, A. Tajima, and R. Kato, Phys. Rev. Lett. 99, 256403 (2007).

[32] T. Itou, A. Oyamada, S. Maegawa, K. Kubo, H. M. Yamamoto, and R. Kato, Phys. Rev. B 79, 174517 (2009).

[33] A. Tanaka and X. Hu, Phys. Rev. Lett. **91**, 257006 (2003).

[34] G. Baskaran, Phys. Rev. Lett. **91**, 097003 (2003).

[35] Q. Han, Z. D. Wang, Q.-H. Wang, and T. Xia, Phys. Rev. Lett. **92**, 027004 (2004).

[36] J. Y. Gan, Yan Chen, and F. C. Zhang, Phys. Rev. B **74**, 094515 (2006).

[37] K. S. Chen, Z. Y. Meng, U. Yu, S. Yang, M. Jarrell, and J. Moreno, Phys. Rev. B **88**, 041103(R) (2013).

[38] K. Takada, H. Sakurai, E. Takayama-Muromachi, F. Izumi, R. A. Dilanian, and T. Sasaki, Nature (London) **422**, 53 (2003).

[39] T. Fujimoto, G. Q. Zheng, Y. Kitaoka, R. L. Meng, J. Cmaidalka, and C. W. Chu, Phys. Rev. Lett. **92**, 047004 (2004).

[40] M. M. Maśka, M. Mierzejewski, B. Andrzejewski, M. L. Foo, R. J. Cava, and T. Klimczuk, Phys. Rev. B **70**, 144516 (2004).

[41] W. Higemoto, K. Ohishi, A. Koda, S. R. Saha, R. Kadono, K. Ishida, K. Takada, H. Sakurai, E. Takayama-Muromachi, and T. Sasaki, Phys. Rev. B **70**, 134508 (2004).

[42] Y. Ihara, K. Ishida, C. Michioka, M. Kato, K. Yoshimura, K. Takada, T. Sasaki, H. Sakurai, and E. Takayama-Muromachi, J. Phys. Soc. Jpn. **73**, 2069 (2004).

[43] M. Kato, C. Michioka, T. Waki, Y. Itoh, K. Yoshimura, K. Ishida, H. Sakurai, E. Takayama-Muromachi, K. Takada, and T. Sasaki, J. Phys.: Condens. Matter **18**, 669 (2006).

[44] M. L. Foo, R. E. Schaak, V. L. Miller, T. Klimczuk, N. S. Rogado, Y. Wang, G. C. Lau, C. Craley, H. W. Zandbergen, N. P. Ong, and R. J. Cava, Solid State Commun. **127**, 33 (2003).

[45] D. P. Chen, H. C. Chen, A. Maljuk, A. Kulakov, H. Zhang, P. Lemmens, and C. T. Lin, Phys. Rev. B **70**, 024506 (2004).

[46] R. Kato, A. Tajima, A. Nakao, and M. Tamura, J. Am. Chem. Soc. **128,** 10016 (2006).

[47] M. Tamura, A. Nakao, and R. Kato, J. Phys. Soc. Jpn. **75**, 093701 (2006).

[48] M. Tamura, Y. Ishii, and R. Kato, J. Phys.: Condens. Matter **19**, 145239 (2007).

[49] Y. Ishii, M. Tamura, and R. Kato, J. Phys. Soc. Jpn. **76**, 033704 (2007).

[50] M. Tinkham, Introduction to Superconductivity, 2nd ed. (Dover, New York, 2004).

[51] W. E. Lawrence and S. Doniach, in Proceedings of the 12th International Conference on Low Temperature Physics, edited by E. Kanda (Keikagu, Tokyo, 1971).

[52] R. A. Klemm, A. Luther, and M. R. Beasley, Phys. Rev. B **12**, 877 (1975).

[53] T. Schneider and A. Schmidt, Phys. Rev. B **47**, 5915 (1993).

[54] R. Marcon, E. Silva, R. Fastampa, and M. Giura, Phys. Rev. B **46**, 3612 (1992).

[55] J. R. Clem, M. W. Coffey, and Z. Hao, Phys. Rev. B **44,** 2732 (1991).

[56] U. Welp, W. K. Kwok, G. W. Crabtree, K. G. Vandervoort, and J. Z. Liu, Phys. Rev. B **40**, 5263 (1989).

[57] D. E. Farrell, J. P. Rice, D. M. Ginsberg, and J. Z. Liu, Phys. Rev. Lett. **64**, 1573 (1990).

[58] J. Hagel, S. Wank, D. Beckmann, J. Wosnitza, D. Schweitzer, W. Strunz, and M. Thumfart, Physica C **291**, 213 (1997).

[59] W. K. Kwok, U. Welp, K. D. Carlson, G. W. Crabtree, K. G. Vandervoort, H. H. Wang, A. M. Kini, J. M. Williams, D. L. Stupka, L. K. Montgomery, and J. E. Thompson, Phys. Rev. B **42**, 8686(R) (1990).

[60] K. Murata, H. Yoshino, H. O. Yadav, Y. Honda, and N. Shirakawa, Rev. Sci. Instrum. **68**, 2490 (1997).

[61] P. A. Mansky, P. M. Chaikin, and R. C. Haddon, Phys. Rev. Lett. **70**, 1323 (1993).

[62] M. Tinkham, Phys. Rev. **129**, 2413 (1963).

[63] K. Kanoda (private communication).

[64] T. Komatsu, N. Matsukawa, T. Inoue, and G. Saito, J. Phys. Soc. Jpn. **65**, 1340 (1996).

[65] K. Nakamura, Y. Yoshimoto, T. Kosugi, R. Arita, and M. Imada, J. Phys. Soc. Jpn. **78**, 083710 (2009).

[66] K. Nakamura, Y. Yoshimoto, and M. Imada, Phys. Rev. B **86**, 205117 (2012).

[67] Y. Shimizu, H. Kasahara, T. Furuta, K. Miyagawa, K. Kanoda, M. Maesato, and G. Saito, Phys. Rev. B **81**, 224508 (2010).

[68] Y. Kurosaki, Y. Shimizu, K. Miyagawa, K. Kanoda, and G. Saito, Phys. Rev. Lett. **95**, 177001 (2005).

[69] E. Scriven and B. J. Powell, Phys. Rev. B **80**, 205107 (2009).

[70] A. E. Underhill, R. A. Clark, I. Marsden, M. Allan, R. H. Friend, H. Tajimas, T. Naito, M. Tamura, H. Kuroda, and A. Kobayashi, J. Phys.: Condens. Matter **3**, 933 (1991).

[71] T. Tsumuraya, H. Seo, M. Tsuchiizu, R. Kato, and T. Miyazaki, J. Phys. Soc. Jpn. **82**, 033709 (2013).

[72] Y. Shimizu and R. Kato, Phys. Rev. B **97**, 125107 (2018).

[73] G. Blatter, M. V. Feigel'man, V. B. Geshkenbein, A. I. Larkin, and V.M. Vinokur, Rev. Mod. Phys. **66**, 1125 (1994).

[74] G. Grüner, Rev. Mod. Phys. **60**, 1129 (1988).

[75] J. A. Krumhansl and J. R. Schrieffer, Phys. Rev. B **11**, 3535 (1975).

[76] H. Fukuyama, J. Kishine, and M. Ogata, J. Phys. Soc. Jpn. **86**, 123706 (2017).

[77] A. W. Hunt, P. M. Singer, K. R. Thurber, and T. Imai, Phys. Rev. Lett. **82**, 4300 (1999).

[78] P. M. Singer, A. W. Hunt, A. F. Cederström, and T. Imai, Phys. Rev. B **60**, 15345 (1999).

[79] N. J. Curro, P. C. Hammel, B. J. Suh, M. Hücker, B.Büchner, U. Ammerahl, and A. Revcolevschi, Phys. Rev. Lett. **85**, 642 (2000).

[80] S. A. Kivelson, I. P. Bindloss, E. Fradkin, V. Oganesyan, J. M. Tranquada, A. Kapitulnik, and C. Howald, Rev. Mod. Phys. **75**, 1201 (2003).

[81] J. A. Bonetti, D. S. Caplan, D. J. Van Harlingen, and M. B. Weissman, Phys. Rev. Lett. **93**, 087002 (2004).

[82] T. Imai, K. Yoshimura, T. Uemura, H. Yasuoka, and K. Kosuge, J. Phys. Soc. Jpn. **59**, 3846 (1990).

[83] P. M. Singer and T. Imai, Phys. Rev. Lett. **88**, 187601 (2002).

[84] M.-H. Julien, A. Campana, A. Rigamonti, P. Carretta, F. Borsa, P. Kuhns, A. P. Reyes, W. G. Moulton, M. Horvatić, C. Berthier, A. Vietkin, and A. Revcolevschi, Phys. Rev. B **63**, 144508 (2001).

[85] G. V. M. Williams, H. K. Lee, and S. K. Goh, Phys. Rev. B **71**, 014515 (2005).

[86] G. V. M. Williams, J. Haase, M.-S. Park, K. H. Kim, and S.-I. Lee, Phys. Rev. B **72**, 212511 (2005).

[87] F. M. Hess, R. D. Merithew, M. B. Weissman, Y. Tokura, and Y. Tomioka, Phys. Rev. B **63**, 180408(R) (2001).

[88] R. D. Merithew, M. B. Weissman, F. M. Hess, P. Spradling, E. R. Nowak, J. O'Donnell, J. N. Eckstein, Y. Tokura, and Y. Tomioka, Phys. Rev. Lett. **84**, 3442 (2000).

[89] P. Dai, J. A. Fernandez-Baca, N. Wakabayashi, E. W. Plummer, Y. Tomioka, and Y. Tokura, Phys. Rev. Lett. **85**, 2553 (2000).

[90] R. H. Heffner, J. E. Sonier, D. E. MacLaughlin, G. J. Nieuwenhuys, G. Ehlers, F. Mezei, S.W. Cheong, J.S. Gardner, and H. Röder, Phys. Rev. Lett. **85**, 3285 (2000).

[91] R. H. Heffner, D. E. MacLaughlin, G. J. Nieuwenhuys, T. Kimura, G. M. Luke, Y. Tokura, and Y. J. Uemura, Phys. Rev. Lett. **81**, 1706 (1998).

[92] V. Podzorov, M. Uehara, M. E. Gershenson, T. Y. Koo, and S-W. Cheong, Phys. Rev. B **61**, R3784(R) (2000).

[93] G. Allodi, R. De Renzi, M. Solzi, K. Kamenev, G. Balakrishnan, and M. W. Pieper, Phys. Rev. B **61**, 5924 (2000).

[94] R. H. Heffner, L. P. Le, M. F. Hundley, J. J. Neumeier, G. M. Luke, K. Kojima, B. Nachumi, Y. J. Uemura, D. E. MacLaughlin, and S -W. Cheong, Phys. Rev. Lett. **77**, 1869 (1996).

[95] E. Dagotto, Science **309**, 257 (2005).

[96] T. A. Witten and P. A. Pincus, Structured Fluids: Polymers, Colloids, Surfactants (Oxford University Press, Oxford, 2010).

[97] J. Schmalian and P. G. Wolynes, MRS Bull. **30**, 433 (2005).

[98] T. Itou, E. Watanabe, S. Maegawa, A. Tajima, N. Tajima, K. Kubo, R. Kato, and K. Kanoda, Sci. Adv. **3**, e1601594 (2017).

[99] T. Sasaki, Crystals **2**, 374 (2012).

[100] M. Ito, T. Uehara, H. Taniguchi, K. Satoh, Y. Ishii, and I. Watanabe, J. Phys. Soc. Jpn. **84**, 053703 (2015).

[101] N. Yoneyama, T. Sasaki, N. Kobayashi, K. Furukawa, and T. Nakamura, Physica (Amsterdam) **405B**, S244 (2010).

[102] L. Kang, K. Akagi, K. Hayashi, and T. Sasaki, Phys. Rev. B **95**, 214106 (2017).

[103] T. Furukawa, K. Miyagawa, T. Itou, M. Ito, H. Taniguchi, M. Saito, S. Iguchi, T. Sasaki, and K. Kanoda, Phys. Rev. Lett. **115**, 077001 (2015).

[104] K. Sano, T. Sasaki, N. Yoneyama, and N. Kobayashi, Phys. Rev. Lett. **104**, 217003 (2010).

[105] B. L. Henke, E. M. Gullikson, and J. C. Davis, At. Data Nucl. Data Tables **54**, 181 (1993).

[106] S. M. De Soto, C. P. Slichter, A. M. Kini, H. H. Wang, U. Geiser, and J. M. Williams, Phys. Rev. B **52**, 10364 (1995).

[107] A. Abragam, Principles of Nuclear Magnetism (Oxford University Press, London, 1962).

[108] F. Kagawa, Y. Kurosaki, K. Miyagawa, and K. Kanoda, Phys. Rev. B **78**, 184402 (2008).

[109] A. Kawamoto, K. Miyagawa, Y. Nakazawa, and K. Kanoda, Phys. Rev. B **52**, 15522 (1995).

[110] X. Su, F. Zuo, J. A. Schlueter, M. E. Kelly, and J. M. Williams, Phys. Rev. B **57**, R14056 (1998).

[111] M. A. Tanatar, T. Ishiguro, T. Kondo, and G. Saito, Phys. Rev. B **59**, 3841 (1999).

[112] J. Müller, M. Lang, F. Steglich, J. A. Schlueter, A. M. Kini, and T. Sasaki, Phys. Rev. B **65**, 144521 (2002).

[113] N. Yoneyama, T. Sasaki, N. Kobayashi, Y. Ikemoto, and H. Kimura, Phys. Rev. B **72**, 214519 (2005).

[114] H. Taniguchi, K. Kanoda, and A. Kawamoto, Phys. Rev. B **67**, 014510 (2003).

[115] M. Matsumoto, Y. Saito, and A. Kawamoto, Phys. Rev. B **90**, 115126 (2014).

[116] F. Kagawa, K. Miyagawa, and K. Kanoda, Nat. Phys. **5**, 880 (2009).

[117] K. Miyagawa, A. Kawamoto, and K. Kanoda, Phys. Rev. Lett. **89**, 017003 (2002).

[118] R. B. Griffiths, Phys. Rev. Lett. **23**, 17 (1969).

[119] T. Vojta, AIP Conf. Proc. **1550**, 188 (2013).

[120] V. Dobrosavljević and G. Kotliar, Phys. Rev. Lett. **78**, 3943 (1997).

[121] M. C. O. Aguiar, V. Dobrosavljević, E. Abrahams, and G. Kotliar, Phys. Rev. B **71**, 205115 (2005).

[122] E. C. Andrade, E. Miranda, and V. Dobrosavljević, Phys. Rev. Lett. **102**, 206403 (2009).

[123] See, V. Dobrosavljević, N. Trivedi, and J. M. Valles, Conxxzductor-Insulator Quantum Phase Transitions (Oxford University Press, Oxford, 2012) and references cited therein.

[124] E. Gati, U. Tutsch, A. Naji, M. Garst, S. Köhler, H. Schubert, T. Sasaki, and M. Lang, Crystals **8**, 38 (2018).

[125] M. Urai, T. Furukawa, Y. Seki, K. Miyagawa, T. Sasaki, H. Taniguchi, and K. Kanoda, Phys. Rev. B **99**, 245139 (2019).

[126] V. Dobrosavljević, T. R. Kirkpatrick, and G. Kotliar, Phys. Rev. Lett. **69**, 1113 (1992).

[127] O. O. Bernal, D. E. MacLaughlin, H. G. Lukefahr, and B. Andraka, Phys. Rev. Lett. **75**, 2023 (1995).

[128] E. Miranda, V. Dobrosavljević, and G. Kotliar, Phys. Rev. Lett. **78**, 290 (1997).

[129] E. Miranda and V. Dobrosavljević, Phys. Rev. Lett. **86**, 264 (2001); Rep. Prog. Phys. **68**, 2337 (2005).

[130] M. C. O. Aguiar, E. Miranda, and V. Dobrosavljević, Phys. Rev. B **68**, 125104 (2003).

[131] D. Tanasković, E. Miranda, and V. Dobrosavljević, Phys. Rev. B **70**, 205108 (2004).

[132] D. Tanasković, V. Dobrosavljević, and E. Miranda, Phys. Rev. Lett. **95**, 167204(2005).

[133] M. C. O. Aguiar and V. Dobrosavljević, Phys. Rev. Lett. **110**, 066401 (2013).

[134] W. S. Oliveira, M. C. O. Aguiar, and V. Dobrosavljević, Phys. Rev. B **89**, 165138 (2014).

[135] R.K. Kaul and M. Vojta, Phys. Rev. B **75**, 132407 (2007).

[136] S. Sen, N. S. Vidhyadhiraja, and M. Jarrell, Phys. Rev. B **98**, 075112 (2018).

[137] M. Sasaki, A. Ohnishi, T. Kikuchi, M. Kitaura, K. S. Kim, and H. J. Kim, Phys. Rev. B **82**, 224416 (2010).

[138] R. Hu, K. Wang, H. Ryu, H. Lei, E. S. Choi, M. Uhlarz, J. Wosnitza, and C. Petrovic, Phys. Rev. Lett. **109**, 256401 (2012).

[139] E. C. Andrade, A. Jagannathan, E. Miranda, M. Vojta, and V. Dobrosavljević, Phys. Rev. Lett. **115**, 036403 (2015).

[140] D. Gnida, Phys. Rev. B **97**, 081112(R) (2018).